
Wesleyan University

A Clever Title

by

Jonas Powell
Class of 2019

A thesis submitted to the
faculty of Wesleyan University
in partial fulfillment of the requirements for the
Degree of Master of Arts

Middletown, Connecticut

April, 2018

*If people sat outside and looked at the stars each night,
I'll bet they'd live a lot differently.*

—CALVIN & HOBBES

Contents

1	Introduction	1
1.1	Submillimeter Observations	4
1.1.1	Interferometry	5
1.1.2	Continuum Emission	12
1.1.3	Line Emission	13
1.2	Disk & The Role of Environment	17
1.2.1	The Minimum Mass (Extra-)Solar Nebula	18
1.2.2	Low- and High-Mass Star Forming Regions	19
1.3	d253-1536: A Misaligned Binary System	23
1.3.1	Local Environment & Features	24
1.3.2	Previous Observations	25
1.4	Summary of Contents	27
2	Observations	29
3	Results	31
3.1	Cloud Contamination	31
3.2	Line Data	35
4	Analysis	39
4.1	Gas Model	39
4.1.1	Establishing Physical Profiles	40
4.1.2	Generating a Model Image	43
4.2	Exploring Parameter Space	45
4.2.1	Grid Search	45

4.2.2	Markov Chain Monte Carlo	46
4.3	Fitting Procedure	49
4.3.1	HCO^+ (4-3) Fit	51
4.3.2	HCN (4-3) Fit	51
4.3.3	CO (3-2) Fit	53
5	Discussion	61
5.1	Planet-Forming Potential	61
5.2	Dynamical Mass of a PMS Star	62
5.3	Best Fit Temperature	62
5.4	HCO^+ , HCN Abundance Structures	62
6	Summary	63
Bibliography		64

List of Figures

- | | | |
|--------------------|---|---|
| 1.1 | An edge-on slice of a protoplanetary disk is presented (Dullemond & Monnier 2010). As is visible in this graphic, significant radial segmentation of the disk exists, particularly between the inner gas disk and outer disk of gas, dust, and planetesimals. Also of note is the large vertical flaring that occurs at large radii. Since the observations that this thesis are based on were made with ALMA (discussed in §1.1.1), we are sensitive primarily to the outer reaches of the disk. | 3 |
| 1.2 | Two example SEDs, accompanied by cartoon models to illustrate the various contributions of different elements of a disk and their influences on the SED (Hughes 2010). The dashed line corresponds to emission from the stellar photosphere, while the colored lines are blackbody curves corresponding to emission from regions of the disk with different temperatures. Since radio observations take place at longer (hundreds to thousands of microns) wavelengths, one may easily see that the stellar contribution in that regime is minimal. . | 6 |
| 12figure.caption.5 | | |

1.5 An example of a moment-one map of a protoplanetary disk, drawn from Rosenfeld et al. (2012). Colors correspond to intensity-weighted velocity; in other words, how quickly material is moving relative to the observer. One may consider this analogously to a spinning Frisbee, approaching the reader edge-on, where one half of the disk is spinning outwards (away from us) as the other side approaches. From this image, we immediately gain several pieces of information: for example, in this case, the disk as a whole is receding from view (since the velocity's "zero point", in yellow/green, is moving at 3 km/s), and that the disk's eastern half is spinning away from us, while the western half comes towards us. This gives us a quick understanding of the disk's kinematics.	15
1.6 Proplyds in the Orion Nebula. The closer a proplyd is to a large, bright star, the more visibly windswept it is. Image courtesy of the Hubble Space Telescope Treasury Program on the Orion Nebula (Robberto et al. (2013))	20
1.8 <i>Left:</i> The masses of 70 ONC proplyds are plotted against their projected distance from the Orion Nebula's central O-star, θ^1 Ori C, drawn from surveys from ALMA and the SMA (Mann et al. 2014). Grey markers indicate 3σ upper limits for non-detections. The dashed line at $10 M_{Jup}$ indicates the minimum-mass solar nebula. As is clear from this plot, a statistically-significant correlation was found between disk mass and distance from θ^1 Ori C. <i>Right:</i> Radius is also affected by proximity to θ^1 Ori C (Eisner et al. 2018) . . .	25

1.10	Images of V2434 Ori taken from Smith et al. (2005) on HST (Fig. 1.9a), Mann & Williams (2009) with the SMA at 880 μ m (Fig. 1.9b), and Ricci et al. (2011) with the EVLA at 7mm (Fig. 1.9c). The ionization front is clearly visible in both the HST and EVLA observations, and the jet from disk A is visible in the HST image.	26
1.12	Moment-1 maps of $\text{HCO}^+(4-3)$, $\text{HCN}(4-3)$, $\text{CO}(3-2)$, and $\text{CS}(7-6)$ emission (left to right) in the present study's proplyds. Each map shows intensity-weighted velocity, which allows us to trace the disks' kinematics. Observed with ALMA's Band 7 receiver	27
3.1	HCO^+ Noise profiles	34
3.2	HCN Noise profiles	34
3.3	CO Noise profiles	34
3.4	CS Noise profiles	34
3.5	Zeroth moment map of CO emission, with and without a cut of all baseline's below $60 \text{ k}\lambda$ (left and right, respectively). Colors correspond to velocity-integrated intensity, while contours represent $\pm 3, 5, 7 \dots 15\sigma$ transitions where 1σ is $0.257 \text{ Jy beam}^{-1} \text{ km s}^{-1}$. Negative contours are dashed. The beam is shown in the bottom left corner, with a diameter of $0.^{\circ}5$ which corresponds to 200 AU at 389 parsec.	36
3.6	First moment map of CO emission, with and without a cut of all baseline's below $60 \text{ k}\lambda$ (left and right, respectively). Colors correspond to intensity-weighted LSRK velocity, while contours represent $\pm 3, 5, 7 \dots, 15\sigma$ transitions where 1σ is $0.257 \text{ Jy beam}^{-1} \text{ km s}^{-1}$	36

3.7 A PV diagram of disk A's HCO ⁺ emission. Some asymmetries are readily noticeable.	38
4.1 Radial and vertical temperature structures for disk A (<i>left</i>) and disk B (<i>right</i>) in CO. We may quickly see that disk A has a larger radial extent and a better defined profile, thanks to its higher signal.	43
4.2 Since disk A and B's features are assumed to be independent, we may generate corner plots for each of their parameter spaces individually. Some analysis REWORK when new plots are added.	48
4.3 Data, model, and residual maps are presented.	55
4.4 Data, model, and residual maps are presented.	56
4.5 Since disk A and B's features are assumed to be independent, we may generate corner plots for each of their parameter spaces individually. Some analysis REWORK when new plots are added.	57
4.6 Since disk A and B's features are assumed to be independent, we may generate corner plots for each of their parameter spaces individually. Some analysis REWORK when new plots are added.	58
4.7 Since disk A and B's features are assumed to be independent, we may generate corner plots for each of their parameter spaces individually. Some analysis REWORK when new plots are added.	59
4.8 Since disk A and B's features are assumed to be independent, we may generate corner plots for each of their parameter spaces individually. Some analysis REWORK when new plots are added.	60
4.9 Disk structure	60
4.10 Disk structure	60
4.11 Disk structure	60

Chapter 1

Introduction

Planetary systems, including our own Solar System, are born from circumstellar disks of gas and dust around young stars. Young ($\leq 10\text{Myr}$) circumstellar disks, known as protoplanetary disks, are easily distinguishable from their older siblings by their large abundance of gas, which typically outweighs the disk's dust by a factor of 100. However, as these disks age they are influenced by gravitational, chemical, and viscous forces, and their gas almost entirely dissipates as they become debris disks, much like our familiar local Solar System's Kuiper Belt and asteroid belt. But while we can observe with relative ease the current state of our local planetary system and debris disks, understanding the process that brought us here is much more difficult. To do so, we must understand the nature of our own disk at its birth, and whether or not that process is a common one that we would expect to see replicated elsewhere. Unraveling this mystery requires that we turn to observations of other comparable protoplanetary disks in order to develop a coherent narrative of disk evolution and, consequently, the conditions necessary for the formation of planetary systems like our own.

To understand the birth of our protoplanetary disk, we must understand the birth of our Sun, as the two are intimately related. Stars form when a region of a molecular cloud develops a gravitational instability sufficient to lead to a runaway collapse (F. Shu, F. Adams 1987), helped along by macroscopic turbulence in the

cloud (McKee & Ostriker 2007). In this process, the cloud shrinks by a factor of around ten million on its way down to a star, analogous to shrinking a square the approximate size of Connecticut ($\sim 150 \times 150$ km) down to just 15mm on each side. Angular momentum, defined as the product of a system's mass, velocity, and radial extent, must be conserved throughout this process, leading to a tremendous increase in the collapsing cloud's angular velocity. As the local material begins to self-gravitate, its center forms a dense core which will eventually become a young star¹.

However, if that angular momentum is conserved only through an increase in angular velocity, those velocities will become so large that the star itself will be unable to form, as centrifugal forces pulling outward will become more significant than the gravitation pulling the star in on itself. In order to prevent velocities from becoming this high, stellar jets and disks, made from the collapsing material, will develop to decentralize the system's mass and dissipate its angular momentum.

The resulting disks present flared radial structures, typically extending several hundred AU (Vicente & Alves 2005). Since these disks form directly out of the collapse process, they, like their stellar host and the initial molecular cloud, are initially composed almost exclusively of molecular hydrogen, although their chemical evolution is significant and heavily studied². Temperatures in their outer reaches are typically in the range of 10-100 K; gas masses are inferred to range from ones to tens of Jovian masses (Andrews & Williams 2005), although this value comes with significant assumptions that are discussed in depth in §1.1.2. Masses for the disks in the present study are calculated in Chapter 3.

¹binaries are also a common outcome in this process; according to Duchêne & Kraus (2013), approximately half of all stars are found in binary systems.

²Improving our understanding of this chemical evolution is also one of the motivating drives of this thesis.

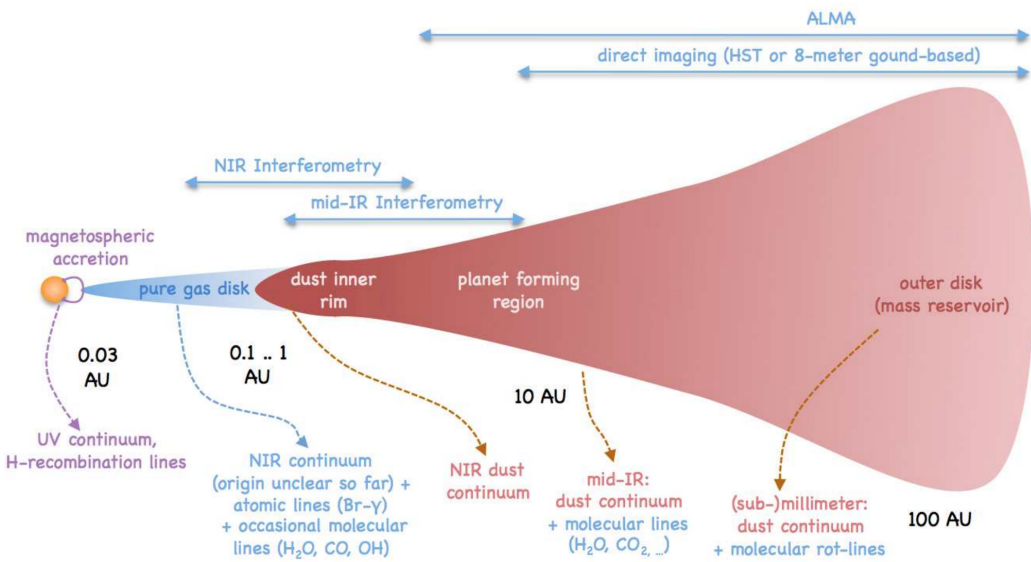


Figure 1.1: An edge-on slice of a protoplanetary disk is presented (Dullemond & Monnier 2010). As is visible in this graphic, significant radial segmentation of the disk exists, particularly between the inner gas disk and outer disk of gas, dust, and planetesimals. Also of note is the large vertical flaring that occurs at large radii. Since the observations that this thesis are based on were made with ALMA (discussed in §1.1.1), we are sensitive primarily to the outer reaches of the disk.

By around 10-20 Myr, the primordial gas and dust in these disks becomes depleted through several processes, including accretion onto the host star, blowing out from radiation pressure, and becoming locked up in icy bodies, transitioning the disk from a protoplanetary disk to a debris disk. These new debris disks are made up of what is thought to be second generation dust, created by the grinding down of boulders and planetesimals, since any primordial dust from the initial collapse should have been blown out by this time. The gas masses in debris disks tend to be orders of magnitude lower than in protoplanetary disks. For a more complete review of disk evolution, see Hughes et al. (2018).

1.1 Submillimeter Observations

Although protoplanetary disks' masses are dominated by gas, they still have sufficient dust to be optically thick in the optical. Consequently, mass measurements are not possible at optical wavelengths. However, since the optical depth of the dust at millimeter wavelengths is low, and since the emission being observed at these wavelengths is thermal rather than due to scattering (as it is in the optical), observations at millimeter wavelengths are preferred for measuring a disk's dust mass. In the radio, we may trace two types of emission:

- **CONTINUUM EMISSION:** Although the size distribution of grains in a dust disk is wide and heavily weighted towards smaller grains, larger, millimeter-sized grains are still present in disks. These larger grains are far more efficient emitters in the radio, since the wavelength of a grain's peak thermal emission efficiency is approximately equal to its size. Thus, we may observe this continuum emission (so named thanks to the wide range of frequencies that thermal emission covers) from these millimeter-sized grains.

- LINE EMISSION: Because radial disk temperatures quickly fall below the temperatures required to cause photodissociation, molecules may live a stable existence in these disks. Conveniently, the rotational transitions of small molecules tend to emit at radio frequencies. Observations of the emission from these rotational transitions, known as line emission, can provide us with a wealth of important information, including kinematics, temperature information, disk chemistry and total disk mass.

Notably absent in both forms is emission from the central star, thanks to the fact that stars are extremely weak emitters in the radio regime, since stars are hot and, consequently, have peak emission in the optical³. This makes them very faint relative to the disk's emission at longer (hundreds to thousands of microns) wavelengths. Fig 1.2 (Hughes 2010) presents a spectral energy distribution, or SED, showing emission intensity as a function of wavelength from an imaginary disk system, demonstrating how small the star's flux density is at long wavelengths relative to the disk's contributions.

However, to understand these types of observation, one must first understand the nature of the "telescope" making the observations. What follows is a brief introduction to radio interferometry, followed by more complete explanations of continuum and line emission.

1.1.1 Interferometry

Interferometry is a clever way to make extremely high-resolution observations at long wavelengths without needing to use incredibly large collecting areas. Were

³Why, then, is the dust still bright relative to the star? While it's true that the flux *per area* of the dust is significantly smaller than of the star, the dust has a far greater surface area, allowing it to compensate and still be a bright emitter.

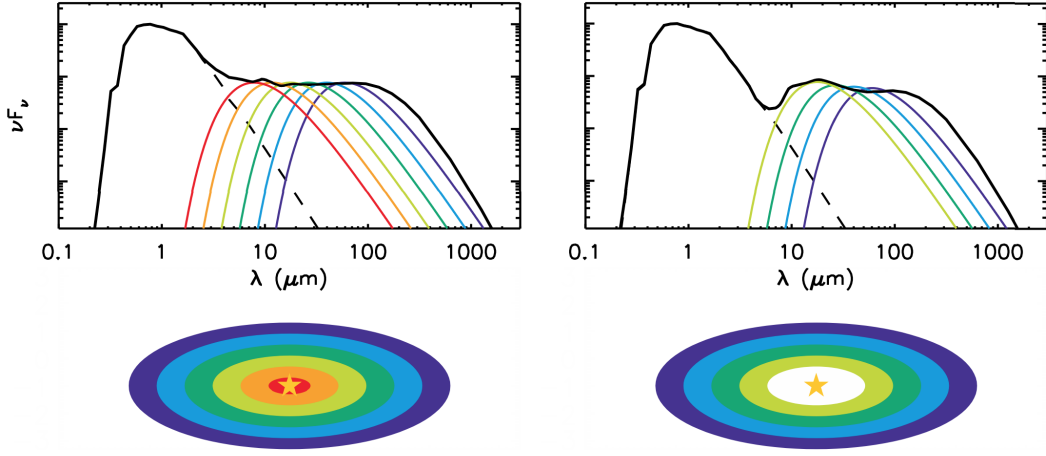


Figure 1.2: Two example SEDs, accompanied by cartoon models to illustrate the various contributions of different elements of a disk and their influences on the SED (Hughes 2010). The dashed line corresponds to emission from the stellar photosphere, while the colored lines are blackbody curves corresponding to emission from regions of the disk with different temperatures. Since radio observations take place at longer (hundreds to thousands of microns) wavelengths, one may easily see that the stellar contribution in that regime is minimal.

one to naively attempt to create a "traditional" (single-aperture) telescope to capture radio emission, they would quickly recall that, for a telescope with a single circular aperture of diameter D , maximum angular resolution is given by

$$\theta = 1.22 \frac{\lambda}{D}, \quad (1.1)$$

where θ is the angular resolution achieved, and λ is the wavelength of the emission being observed. Unfortunately, light in the radio regime has wavelengths on the order of millimeters to centimeters, orders of magnitude longer than optical light, which is in the hundreds of nanometers. Consequently, to achieve a resolution comparable to that of an optical telescope, one would have to increase their aperture's diameter accordingly to match the increase in λ . Some have tried this approach: the Arecibo Observatory in Puerto Rico and the Five hundred

meter Aperture Spherical Telescope in China (with diameters of 300m and 500m, respectively) are two immediate examples, but both still have resolutions ($\sim 25''$ for Arecibo and $\sim 15''$ for FAST, observing 3cm emission) that are too coarse to resolve the length-scales that we would like when observing disks. Building and maintaining apertures this big is also an extreme challenge, usually requiring mountains to be hollowed out, making this an unappealing solution.

The alternative is to leverage the power of interferometry for a solution to the problem. In an interferometric system, one may construct an image using the interference patterns between light received by two or more separate apertures. In this case, the maximum angular resolution becomes inversely proportional to the maximum distance, or *baseline*, between any two apertures, which can be made almost arbitrarily large. Interferometry does come with tradeoffs, however, the most notable of which is in sensitivity, since sensitivity is proportional to collecting area and each dish in an interferometer is typically fairly small. Additionally, interferometers also have inherent spatial filtering, meaning that they are not sensitive to flux from sources covering large angular scales. This is because the largest angular scale of a flux source that a telescope is sensitive to is inversely proportional to its smallest baseline. Since the collecting area of a single-dish telescope is a continuous surface, its smallest "baseline" is essentially infinitely small (making it sensitive to arbitrarily-large flux sources). Conversely, for an interferometer, that smallest baseline is typically ones to tens of meters. Therefore, interferometers are intrinsically unable to capture flux from sources with angular scales larger than λ/D_{\min} .⁴

While this interference process can be done at optical wavelengths with CCDs,

⁴This can actually be an advantage, however, as it offers the opportunity to choose the length-scale being observed, i.e. remove cloud contamination (large scale structure) from an image of a disk (a small structure).

it is far more difficult to execute, as light must be forced to physically interact before reaching the sensor via a complex and extremely precise optical system. At longer wavelengths, however, heterodyne receivers may be used, making the task of interfering the signals a digital process, rather than a physical one. A heterodyne receiver records both the amplitude (analogous to the intensity that a CCD might measure) and the phase of the signal it receives. Because the receiver captures phase information as well as amplitude, the signals from two dishes may be digitally interfered after being received. Physical features must be calibrated out, including phase delay caused by differences in line-of-sight path length from the source between the receivers, atmospheric effects, and instrumental phase delays. The result, for a single baseline, is a complex voltage pattern describing the amplitude and phase of the interference pattern between the signal each dish received. We call this voltage pattern a *visibility*.

The complete output from an interferometer is a collection of these visibilities. Taken together, they approximate the Fourier transform of the sky image. We say that this output lives in the "visibility domain", which itself is a Fourier transform of the image domain. A single visibility relates to the full set of visibilities analogously to the relationship between a pixel and an image.

While the image domain has spatial dimensions (i.e. the xy plane), the visibility domain instead uses the uv plane. The uv plane is a wavelength-scaled $x - y$ coordinate system parallel to the sky in the direction of the target source. Here "wavelength-scaled" can be taken to mean that $u = X/\lambda, v = Y/\lambda$, where λ is the wavelength of observation and X and Y are the lengths of the x and y (i.e. north/south, east/west) components of the projected baseline. Thus, each baseline samples a specific spatial frequency, given by $\theta = 1/\sqrt{u^2 + v^2}$. An interferometer may thus be represented on the uv plane as a scatter of points, with

each point corresponding to the wavelength-scaled, target-projected, component distance between two receivers. The ideal aperture would completely fill the uv plane, so that every spatial frequency was sampled. However, since the number of baselines we may access is very limited (approximately the square of the number of antennae in an array), this is clearly an impossibility for an interferometer.⁵

However, the fact that the *projected* baseline is really what determines visibility's location in the uv plane, rather than the baseline's "true", un-projected length, allows us to cleverly gain far more points in the uv plane than one might immediately expect. Since the Earth rotates throughout the night, the projection of a given baseline relative to the target source will change throughout the night as well. Consequently, by making observations over the course of a night, many more points in the uv plane may be sampled, yielding a better-filled plane. This process is known as "Earth rotation aperture synthesis."

We now consider how one might recover an image from a set of observed visibilities. In general, moving between frequency space and distance space is given by a simple Fourier transform. When applying this translation to telescopes, we consider the shape of the image produced by observation of a single point source directly on axis with the aperture. For a conventional telescope with a circular aperture, coverage in the uv plane is in the shape of a filled circle of constant amplitude. Translation to the image domain, via a Fourier transform of that shape, results in the familiar 2-D Airy Disk, the characteristic point-spread function (PSF) of a single aperture convolved with a point source. With an interferometer, this process would be equally straightforward if the uv plane were fully sampled, but because it is not, the resulting image is instead a Fourier

⁵Of course, a single-aperture telescope does not have this problem since its uv plane is one continuous collecting area and thus can be seen as having infinite baselines and complete uv coverage.

transform of all the points in the uv plane sampled by the baselines, and can take on a very complex shape⁶. However, while this shape is complex, it is still - as is the case in the optical - just a convolution of the point source with some PSF, only in this case the PSF is more complicated than an Airy function. As we increase the number of uv points sampled, the resulting image will increasingly approximate a bumpy and/or elongated Airy disk. In radio astronomy, we call this PSF the "dirty beam".

When observing a source, we would like to find the true sky brightness pattern (i.e. the sky image). As described above, the Fourier transform of a set of visibilities is a convolution of the dirty beam with the true sky brightness pattern. Therefore, we would like to remove the dirty beam's contributions to the image. The process of removing the influence of the dirty beam, and the artifacts it can introduce, is called deconvolution. In practice, this deconvolution process takes the form of some iterative algorithm that selectively removes the effects of the dirty beam. The curious reader is referred to the CLEAN algorithm (Hogbom 1974), the first and most popular deconvolution algorithm (and the one used in this work), as well as the maximum-entropy method (Wernecke & D'Addario 1977; Skilling & Bryan 1984). It is worth noting at this point, however, that due to the artifacting and non-unique result that the imaging process introduces, all of our analysis is performed directly on the visibilities themselves, rather than the image. This means that the specific parametrization of CLEAN or any other step in the imaging process does not need to be perfect, since it is purely diagnostic or expository.

⁶ Additionally, thanks to the incomplete sampling of the uv plane, an infinite number of images could all be consistent with some given finite set of visibilities, although many of them would not be physically possible. The one we choose to look at is determined by our deconvolution process, but is not actually the true image.

In summary, interferometry works by recording amplitude and phase information about some emission with many radio antennae and digitally interfering each antenna's signal with the signal received by every other telescope. Each of the resulting interference patterns is called a visibility, and represents a point in *uv* space. Translation from the visibility domain to the image domain involves taking the Fourier transform of the visibilities and deconvolving the dirty beam's influence.

Currently, the world's most advanced interferometer, and the source of this thesis's data, is the Atacama Large Millimeter/Submillimeter Array (ALMA), shown in Fig 1.3a. Built in the high Chilean desert at around 5,000 meters (16,000 feet), the \$1.4-billion array first opened its eyes for scientific observation in mid-2011, with funding from a global partnership between Chile, the United States, and several other countries. With its 66 total antennae (50 12-m dishes and 16 7-m dishes) and baselines extending out to 15-km, it offers an order of magnitude increase in sensitivity and resolution over previous arrays that observe at similar frequencies, which include the Submillimeter Array (8 6-meter dishes), NOEMA (10 15-meter dishes) and the CARMA (23 dishes of 3.5-m, 6.1-m, and 10.4-m diameters).

The effects of this increase are impressive; gaps and rings in faraway disks are now resolvable in striking clarity (Fig. 1.3b), providing a treasure-trove of opportunity to hone our understanding of disk evolution and planetary-system formation. ALMA has also been a blessing to other subfields of astronomy as well, enabling high-resolution observations of everything from complex organic molecules in disks (Walsh et al. 2016; Podio et al. 2019) to gravitational lensing from dark matter halos (Herrera-Martín et al. 2019) to molecular tori around black holes (Combes et al. 2018). Additionally, as a component of the Event Horizon



Figure 1.4: *Left:* A rendering of ALMA⁷ shows the interferometer’s antennae in the high desert, as well as a purpose-built truck moving one of the antennae (lower right). *Right:* A recent survey from ALMA by Andrews et al. (2018) reveals stunning detail in several protoplanetary disks.

Telescope, ALMA played a key role in imaging a black hole’s event horizon for the first time (Collaboration 2019). These awe-inspiring projects are a small portion of ALMA’s contributions to the world of radio astronomy, and more are being made with each passing day.

With an improved understanding of the mechanics of radio interferometry, we may now revisit continuum and line emission.

1.1.2 Continuum Emission

Continuum emission observations integrate flux from a wide band of frequencies, just as our eyes do in the optical. They are appealing for their simplicity and because, by integrating a wide band, they are sensitive to faint objects.

When observing protoplanetary disks, an understanding of planet formation is often a guiding motivation. One parameter that is critical to the planet-forming process is total disk mass. We know that, to first order, when a disk is optically thin, its total mass, M_{disk} , is linearly proportional to its flux density, F_{ν} (Hildebrand 1983), which is found from an observation of continuum emission. This

relationship is given by

$$M_{\text{disk}} = \frac{F_\nu d^2}{\kappa_\nu B_\nu(T_c)}, \quad (1.2)$$

where d is the source's distance, κ_ν is an assumed dust opacity, and $B_\nu(T_c)$ is the Planck function at a given characteristic temperature, T_c . The value of T_c and disk opacity can be inferred without much difficulty by fitting the disk's SED using a simple model. This function is, of course, rather approximate; it assumes a single temperature and single dust opacity (a function of composition and grain size distributions) throughout the disk. The assumption of optically thin emission means that calculations made will inherently be lower limits, since any substantial optical depth will block emission from inner regions of the disk. Furthermore, even in the case of optically thin emission, significant mass may be locked up in bodies that are invisible to our observations. Still, it is a useful tool that can be used to approximate disk mass using continuum emission images.

1.1.3 Line Emission

As molecules collide with one another or absorb light, they gain energy, entering higher rotational energy states. However, as their presence in these states cannot be sustained without the addition of more energy, they will de-excite soon after. This de-excitation process - stepping down from one rotational energy state to the one below - causes the emission of light. Every transition in every molecule emits at its own specific frequency, or rest frequency, making that light identifiable to observers. We may observe a specific rotational transition from a single type of molecule by tuning our receiver to be sensitive to a very narrow window of fre-

quencies immediately around the rest frequency of the transition of interest. This is known as a spectral window. The narrow range of frequencies at which a given molecular transition emits makes ALMA's large sensitivity particularly crucial for observations of molecular lines at high spectral resolution or in rare species.

One immediate feature that line emission gives us access to is velocity information: since all emission should have a single frequency (the transition's rest frequency), we immediately know that any variation from that central frequency is a result of Doppler shifting caused by line-of-sight velocity⁸. This allows us to make a "moment-one" map of emission, which shows the intensity-weighted velocity structure of the disks (Fig 1.5).

Observations of line emission also give us information about both the temperature and density structures of the disk, since these are the two factors that influence how much emission we observe. However, in the case of optically thin emission, the two are degenerate, since an increase in either one will increase emission intensity. In this case, we may combine observations of multiple species to model the temperature structure of a disk. In the case of an optically thick line, however, the temperature and density are no longer degenerate, since all emission originates from the $\tau = 1$ surface, which removes density from the equation and gives us a value for the temperature at that point in the disk's vertical structure. This is valuable, since the a disk's vertical temperature profile varies significantly, with the surface notably warmer than the midplane.

Besides offering information about radial density and temperature profiles, line emission also provides another way of finding total disk mass. Like the initial cloud that the star and disk formed from, the vast majority of the disk's mass comes

⁸Technically, the uncertainty principle tells us that a line will have some "natural" width, but this width is small compared to the Doppler width.

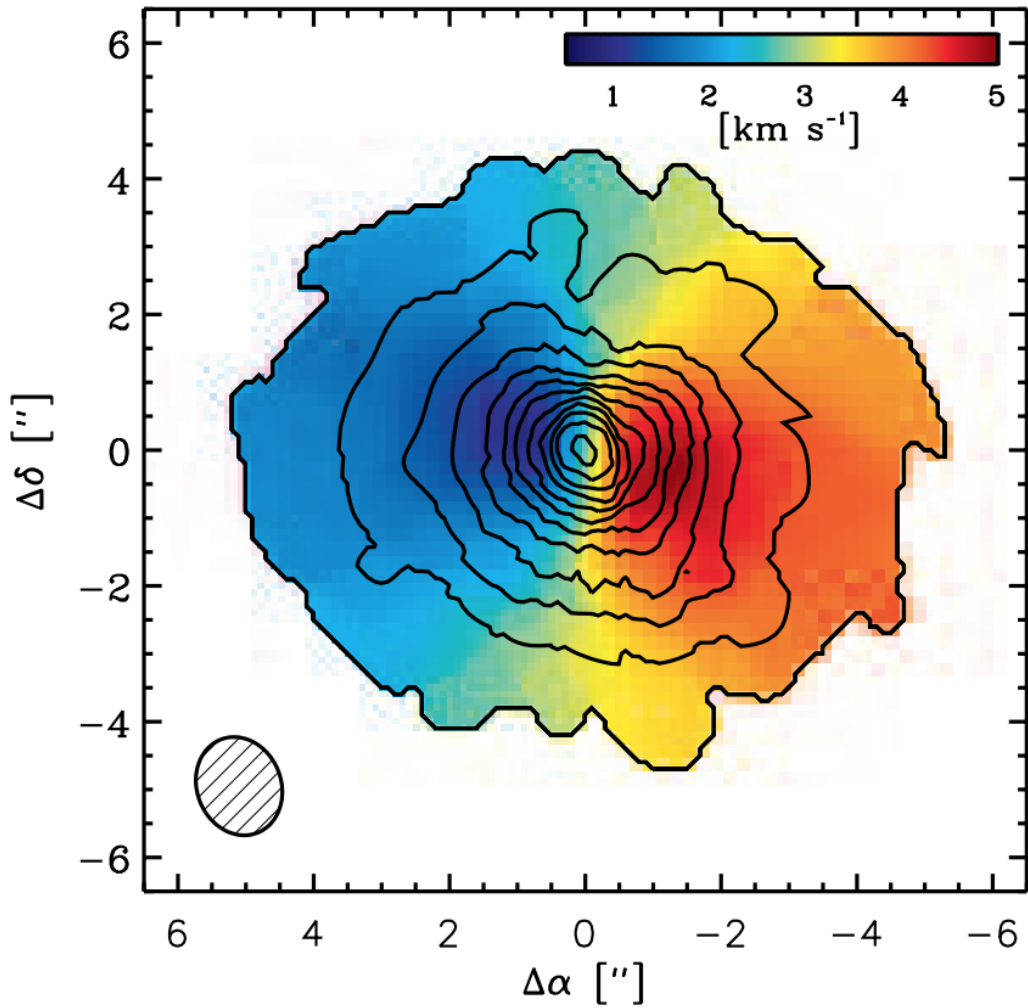


Figure 1.5: An example of a moment-one map of a protoplanetary disk, drawn from Rosenfeld et al. (2012). Colors correspond to intensity-weighted velocity; in other words, how quickly material is moving relative to the observer. One may consider this analogously to a spinning Frisbee, approaching the reader edge-on, where one half of the disk is spinning outwards (away from us) as the other side approaches. From this image, we immediately gain several pieces of information: for example, in this case, the disk as a whole is receding from view (since the velocity's "zero point", in yellow/green, is moving at 3 km/s), and that the disk's eastern half is spinning away from us, while the western half comes towards us. This gives us a quick understanding of the disk's kinematics.

in its gas, and like that initial cloud, the vast majority of that gas is molecular hydrogen, or H₂. However, since H₂ is a symmetric molecule and thus has no permanent dipole moment, it has no rotational transitions and does not emit in the radio, making it invisible to our instruments. As a consequence, we must instead observe emission from other molecules, make assumptions about those molecules' abundances relative to H₂, and extrapolate the total disk mass.

To do so, one generally begins with CO, second most abundant molecule behind H₂. Thanks to its abundance, as well as its relatively low excitation temperature, CO provides robust, bright emission. Drawing on measurements of CO/H₂ ratios in warm dense cloud (Aikawa & Herbst 2003; Fogel et al. 2011), we use a ratio of 1:10000, or 10⁻⁴, to represent CO's relative abundance in protoplanetary disks, while for other, more complex molecules, relative abundances are generally drawn from the interstellar-medium literature and chemical modeling.

However, this CO/H₂ ratio of 10⁻⁴, which is frequently used to calculate disk masses (e.g. Ansdell et al. (2017)) comes with significant uncertainty. Using a gas-grain chemical model Reboussin et al. (2015) showed, through an analysis of CO isotopologues, that at low temperatures (below 30-35K), CO is converted to less volatile molecules (typically s-CO₂ or s-CH₄). This means that below these temperatures, relative CO abundance quickly falls about two magnitudes below the literature value of 10⁻⁴. Schwarz et al. (2016) followed this modeling with high spectrospatial resolution ALMA observations of four CO isotopologues in the nearby protoplanetary disk TW Hya, and confirming a ratio of C/H₂ = 10⁻⁶. Additionally, Yu et al. (2017) notes that CO depletion in the outer disk and optically thick emission from the inner disk has lead observers (e.g. Ansdell et al. (2017), who found surprisingly low disk masses in their survey of ONC proplyds) to underestimate disk mass by more than an order of magnitude if they assume

$\text{CO}/\text{H}_2 = 10^{-4}$ and optically thin emission. They also note that CO abundances change on short (~ 1 Myr) timescales, resulting in a degeneracy between disk age and mass. Ultimately, CO's tight dependence on disk temperature and its evolutionary trends with age increase the need for a well modeled temperature profiles to inform the selection of an appropriate molecular abundance of CO.

1.2 Disks & The Role of Environment

There is significant evidence that most stars in our galaxy (Lada & Lada 2003; Mann et al. 2015), including our own Sun (Gaidos et al. 2009; Tachibana et al. 2006), formed in high-mass star forming regions, or HMSFRs. Therefore, understanding our own creation story necessitates the understanding of protoplanetary disk evolution in these SFRs, and the role that environment plays in that process. However, until ALMA came online in 2012, line-emission studies of disks in these HMSFRs were not feasible, due to the need for increased sensitivity and resolution in the observations.

Now that this telescope is available, however, HMSFRs are open for observation. We may use this opportunity to try to better understand the role that environment plays in the development and evolution of protoplanetary disks, comparing them to the well-studied disk population in low-mass (Andrews & Williams 2005; Mann et al. 2015) and the one well-characterized disk in an HMSFR (Factor et al. 2017), and evaluate how that environment may affect planet-formation potential.

1.2.1 The Minimum Mass (Extra-)Solar Nebula

The minimum-mass solar nebula (MMSN) is a conceptual aid used to inform astronomers about the distribution of material required to form a planetary system (Weidenschilling 1977). The MMSN is the radial mass profile that our own Solar System would present if the mass of each planet were, rather than being bound up in spheres, instead ground up and spread across the ring bound by the orbits of their inferior and superior neighbors. Gas is then added to the ring until its gas:dust ratio reaches the canonical interstellar-medium value of 100:1 (meaning that gas giants like Jupiter would have very little gas mass added, while terrestrial planets like Earth would have their mass significantly increased). The resulting mass profile represents the minimum surface density required to form our own protoplanetary disk and thus a way to inform our comparisons of other disks to our own. When this surface density profile is integrated into a single mass, it gives $M_{\text{MMSN}} = 0.01M_{\odot}$.

It is, of course, an extremely approximate characterization. One significant assumption it makes is that our planets formed in their current positions. This is a statement that we know both to be false (Walsh et al. 2011; Tsiganis et al. 2005) and consequential, since planetary migration can cause disks to lose mass by pushing competing planetesimals either out of orbit or into inner regions of the disk where they may be more susceptible to accreting onto the host star. Another assumption being made is that the chemistry is radially and temporally constant, which is also known to not be the case (van Dishoeck & Blake 1998).

The MMSN model was generalized to be tolerant to a wider diversity of planetary systems by Kuchner (2004) as the minimum-mass extrasolar nebula (MMEN), using 26 Doppler-detected planets in multi-planet systems to construct a disk

analogous to that of the MMSN. Chiang & Laughlin (2013) developed a similar model, this time drawing on Kepler and HARPS planets ($n \approx 10^5$) to explain the existence of close-in ($P < 100$ days) super Earths, which make up approximately half of the planets observed in those catalogues. Both models assume that planets formed at or near their current positions. However, Raymond & Cossou (2014) showed, using 191 multi-planet systems primarily drawn from the Kepler catalogue, that the resulting range of surface density profiles was broad, and thus that using a single, "universal" profile to locate disks with planet-forming potential - as the MMSN/MMEN purports to offer - was not plausible. They note that this broad spread likely reflected the necessity for consideration of planet migration, particularly amongst gas giants.

Still, while the MMSN clearly makes significant assumptions that lead to inconsistencies, it is nonetheless used as an approximate barometer for planet-forming potential.

1.2.2 Low- and High-Mass Star Forming Regions

Thanks to limitations in sensitivity and resolution, most submillimeter surveys in the pre-ALMA epoch focused on young disks in the nearby low-mass SFRs of Taurus-Auriga and ρ Ophiuchus. Dust-emission studies of disks in this regions by Andrews & Williams (2005, 2007) have yielded a wide range of disk masses, with a median of $0.005 M_{\odot}$ and a significant fraction with mass greater than the MMSN. This large fraction of disks with planet-forming potential is consistent with what we would expect based on the enormous - and still growing - number of exoplanets that have been discovered in the last two decades.

Of course, studying only nearby disks paints an incomplete picture of the pop-

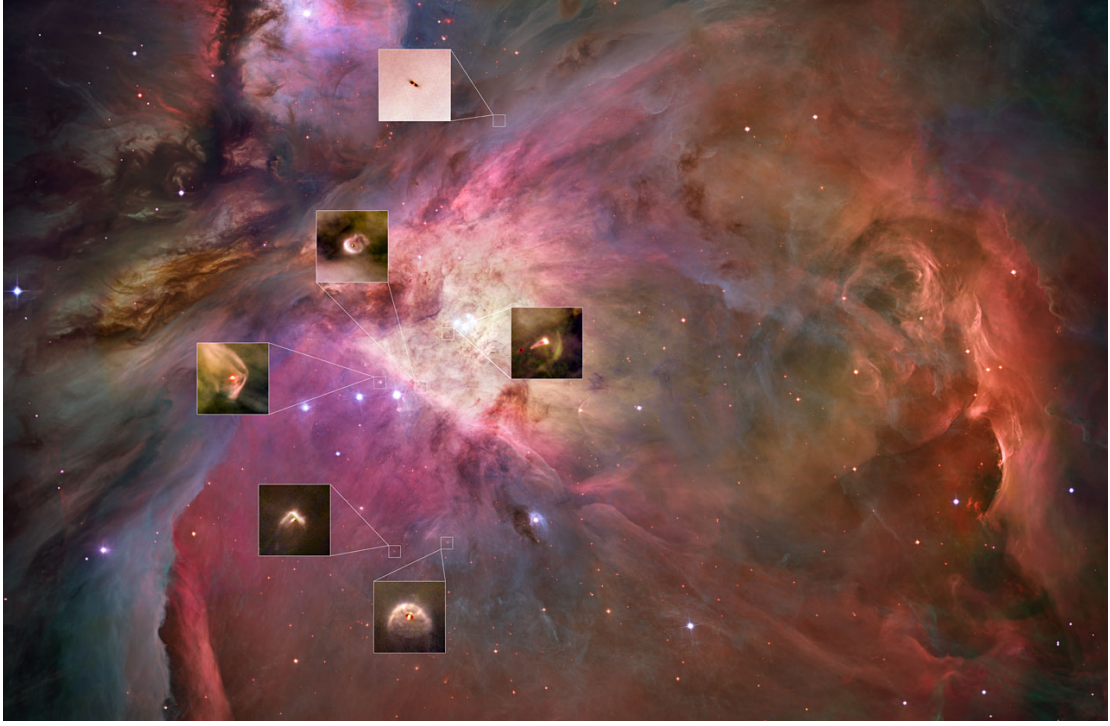


Figure 1.6: Proplyds in the Orion Nebula. The closer a proplyd is to a large, bright star, the more visibly windswept it is. Image courtesy of the Hubble Space Telescope Treasury Program on the Orion Nebula (Robberto et al. (2013))

ulation and its evolutionary trends; for one, most stars form in high-mass SFRs (Lada & Lada 2003; Mann et al. 2015), and low-mass SFRs are qualitatively different than their high-mass siblings. High-mass SFRs are massive, dense clusters with large abundances of high-mass O and B stars. Protoplanetary disks in these regions experience accelerated mass loss, thanks to the powerful ionizing radiation from the high-mass stars (Anderson et al. 2013; Kalyaan et al. 2015; Xiao & Chang 2018). This mass loss is likely a problem for planet formation (Johnstone et al. 1998; Ovelar et al. 2012) and negatively affects potential habitability (Kruijssen & Longmore 2019), but its effects are not yet well understood. It is because of these factors that we would like to study disks in high-mass SFRs.

The nearest high-mass SFR to us is the Orion Nebula Cluster (ONC), 389 pc

away. The Hubble Space Telescope was the first to dedicate significant time to the ONC, producing an abundance of iconic and awe-inspiring images the cluster and of the disks it hosts (Ricci et al. 2008). These studies have guided many subsequent observations, including many in the radio. Many of the cluster’s protoplanetary disks (or proplyds, as those in the ONC are called) are visibly teardrop-shaped, tailing away from the cluster’s biggest, brightest stars. Images like Fig 1.6, showing disks being pushed away from nearby bright stars, and countless others demonstrate the harsh environment that these young disks exist in. Indeed, the influence of these large stars has already been demonstrated, both in their affect on mass-loss rate and mass distribution. Statistically-significant anti-correlations between disk mass and proximity to the ONC’s central O star, θ^1 Ori C, have been shown using both data from the SMA (Mann & Williams 2009) and ALMA (Mann et al. 2014; Ansdell et al. 2017; Eisner et al. 2018).

Furthermore, both observations (Henney & O’Dell 1999) and modeling (Haworth et al. 2016) characterizing mass-loss rates for these proplyds in the Orion Nebula have found rates of $\dot{M} \approx 10^{-7} - 10^{-5} M_{\odot} \text{ yr}^{-1}$, implying that a typical disk (i.e. one of MMSN-scale, or $\sim 0.01 M_{\odot}$) should be fully dispersed before giant planets could form (Hubickyj et al. 2005) and before they could reach the inferred age of the disk-hosting stars in the ONC of ≈ 2 Myr (Reggiani et al. 2011).

Despite all this, not only do we still see disks, but we still see significant planet-forming potential in the Orion Nebula, potential that is comparable to that of other low-mass SFRs. A full 30% of disks surveyed in the ONC have disks with masses greater than or equal to the MMSN (Mann et al. 2014), falling comfortably between ρ Ophiuchus’ 29% Andrews & Williams (2005) and Taurus’ 37% (Andrews & Williams 2007).

However, since all these surveys are based exclusively on the analysis of dust continuum emission, the comparison is profoundly hamstrung by its reliance on assumptions of gas/dust ratios drawn from the ISM literature. This means that the resulting understanding of the gas masses in these regions is directly proportional to that 100:1 gas/dust ratio, a value that is almost certainly not correct. The problem then becomes a matter of understanding how far off it is Yu et al. (2017) suggest it may be closer to 1000:1) and how significantly that ratio varies with environment. The consequences of this assumption are significant, since a disk’s gas mass directly determines its giant planet forming potential both by setting the amount of raw material available to the forming planet as well as by influencing the environment’s turbulence profile and planets’ migratory patterns within the disk. Furthermore, these continuum surveys cannot reveal these disks’ chemistries and the environmental influences that likely affect them, instead simply assuming solar composition. Together, these assumptions regarding both the total gass mass as well as its composition result in a heavy asterisk accompanying any claims we make about the birth and evolution of protoplanetary disks in high-mass SFRs. To solve this, we must understand the chemical make up of these disks, and for that we need studies of line emission.

Mann et al. (2014) made the first line-emission survey of the Orion proplyds as part of ALMA’s Cycle 0 Early Science operation. The survey studied 22 disks in four molecular lines (HCO^+ , HCN, CO, and CS) and $856\mu\text{m}$ continuum, and calculated each disk’s dust mass from the continuum emission. Since then, only one of the disks has had its line data analyzed. Factor et al. (2017) performed an analysis of the radial distribution of one of the disks’ gas by modeling emission from the lines to try to understand the chemical abundance and physical structure of different molecules in the disk. This fitting process was performed on three

of the four molecular lines (as CS had insufficient signal to produce meaningful constraints).

In the study, the authors found several unexpected features: their measurement of the disk's HCN abundance was higher than expected (although HCO^+ and CO abundances were consistent with literature values from low-mass SFRs), their mass measurement for the central star was inconsistent with the previously-determined spectral type, and they found a spatially unresolved high-velocity excess emission feature in the $\text{HCO}^+(4-3)$ and CO(3-2) lines, with a positional offset from the central star. For this emission feature, they found that the source was blue shifted by -6.2 km s^{-1} relative to the systemic velocity, had a position consistent with a $60 \pm 20 \text{ AU}$ Keplerian orbit, and had an inferred H_2 mass of $1.8\text{-}8 \text{ M}_{\text{Jup}}$. They determined that the excess of emission was caused by a local density and/or temperature fluctuation in the inner disk, indicating that it was not a jet or cloud contamination. The authors propose that this could be the result of young Mars-sized bodies, collisions between particles trapped in mean motion resonance by a giant planet, magnetic-field-induced zonal flows, or planet formation.

These unexpected results demonstrate the need for further analysis of disks in this survey. The binary system that is the subject of this thesis is drawn from the same survey, representing the second and third ONC proplyds to have their temperature and density profiles characterized.

1.3 d253-1536: A Misaligned Binary System

The subject of this thesis is the system d253-1536, a binary of pre-main sequence stars in the M43 region of the Orion Nebula Cluster. Each star has its own

proplyd. The stars' projected separation is somewhat atypically wide (approximately 400 AU), and their rotational axes are misaligned. Each star in the system has its own disk, henceforth called disk A and disk B (east and west, respectively, in all images of the system⁹).

1.3.1 Local Environment & Features

Many previous surveys have studied disks in the famous M42, or Orion Nebula, which lies adjacent to M43, and particularly the Trapezium cluster, a region near M42's brightest star O-star θ^1 Ori C. Mann et al. (2014) found a statistically significant correlation between disk mass and distance from θ^1 Ori C in a study of 70 proplyds (Fig. 1.8), particularly within 0.03 pc of the star, where there is a lack of disks more massive than $3M_{\text{jup}}$. These disks are also truncated in radial extent, with no disks extending out past 60 AU in this region (Eisner et al. 2018).

However, because of M43's separation from the Trapezium cluster (it lies ≥ 1 pc to the cluster's north), disks in this region do not experience the same levels of photoevaporation. M43 has only one large emitter, ν Ori, which is a triple-star system whose main component is a B-type star. d253-1536 is wrapped in an ionization bow shock, HH 668 A (1.9a), about 1'' to the system's west and facing towards ν Ori, but otherwise the system shows no signs of influence from giant stars, whether in photoevaporation or in morphological influences (Mann & Williams 2009).

The misalignment of the disks' rotational axes is fairly typical of wide binaries like this one (Williams et al. 2014). The frequency with which these wide binaries present such misalignment indicates that wide binaries likely do not form in large,

⁹The reader will recall that this corresponds to disk A being on the left and disk B on the right of all images, since east and west are inverted in celestial coordinates relative to our familiar geographic ones.

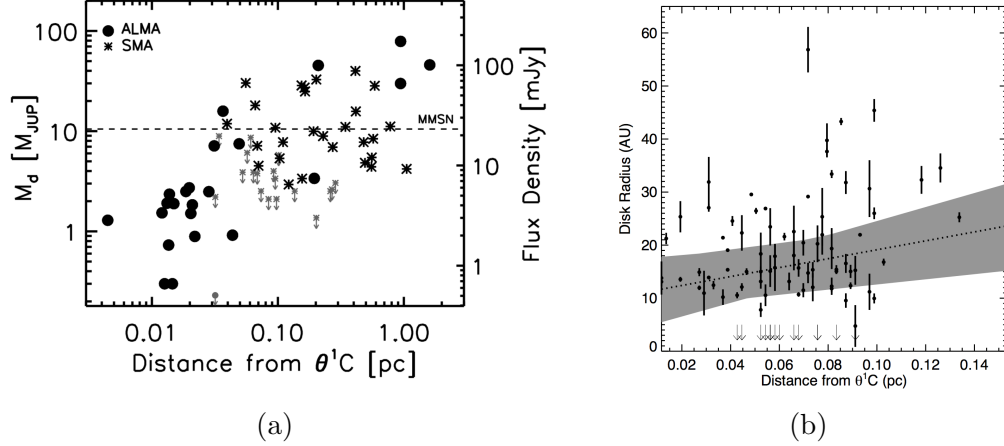


Figure 1.8: *Left:* The masses of 70 ONC proplyds are plotted against their projected distance from the Orion Nebula’s central O-star, θ^1 Ori C, drawn from surveys from ALMA and the SMA (Mann et al. 2014). Grey markers indicate 3σ upper limits for non-detections. The dashed line at $10 M_{Jup}$ indicates the minimum-mass solar nebula. As is clear from this plot, a statistically-significant correlation was found between disk mass and distance from θ^1 Ori C. *Right:* Radius is also affected by proximity to θ^1 Ori C (Eisner et al. 2018)

co-rotating structures, and emphasizes the importance of gas turbulence and interstellar interactions for young stars.

The system’s larger disk, disk A, has a large jet emanating from it in observations in the optical made with HST (Smith et al. 2005). However, since the jet is not visible in the radio, we make no attempt to discuss, model or explain it.

1.3.2 Previous Observations

First observed by Smith et al. (2005) using the Hubble Space Telescope, the authors took interest in what they saw as a binary system containing one star without a disk and one star embedded in a proplyd with a large jet and exhibiting tidal interactions with its companion (Fig 1.9a). Mann & Williams (2009) used 880 μ m continuum measurements to estimate dust masses of the disks to be 0.066 M_\odot and 0.018 M_\odot , for disks A and B respectively, making d253-1536a the most

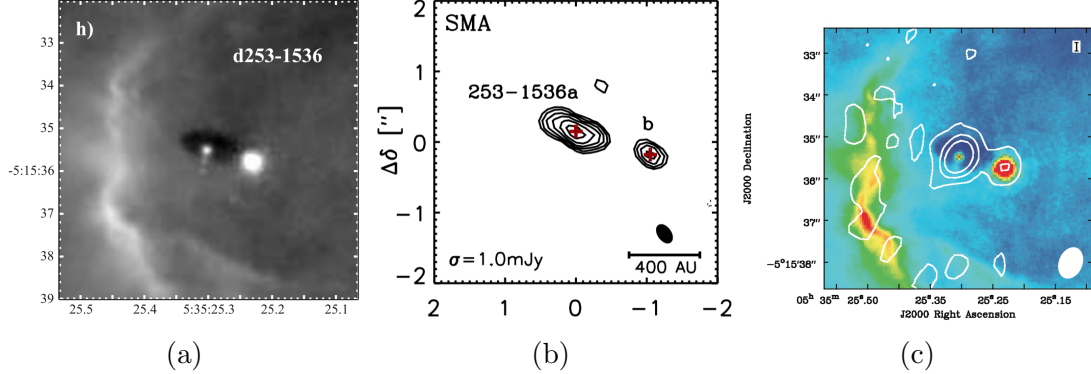


Figure 1.10: Images of V2434 Ori taken from Smith et al. (2005) on HST (Fig. 1.9a), Mann & Williams (2009) with the SMA at 880 μm (Fig. 1.9b), and Ricci et al. (2011) with the EVLA at 7mm (Fig. 1.9c). The ionization front is clearly visible in both the HST and EVLA observations, and the jet from disk A is visible in the HST image.

massive disk measured in the ONC, significantly larger than the Cluster’s second largest disk at $0.034 M_{\odot}$ and adding credence to the theory that θ^1 Ori C is likely responsible for the truncation of disk masses in the Trapezium cluster. Subsequent detections at 7mm by Ricci et al. (2011) indicated that both disks are hosts to substantial populations of large dust grains (1.9c), although the distributions of grain sizes are different in the two disks. The same study also spectral typed the host of d253-1536b to be an M2 star and G2 for d253-1536a’s host star.

The system was observed in an ALMA survey of 22 proplyds in M43 by Mann et al. (2014) in four molecular lines ($\text{HCO}^+(4-3)$, $\text{HCN}(4-3)$, $\text{CO}(3-2)$, and $\text{CS}(7-6)$; Fig ??), and preliminary fits of the system’s kinematics in the $\text{HCO}^+(4-3)$ line were made by Williams et al. (2014). Using continuum observations alone and assuming canonical values for temperature, dust opacity, and gas-to-dust ratio, they found disk masses of $0.074 M_{\odot}$ and $0.028 M_{\odot}$ for disks A and B, respectively, larger than the previous values. They found an inclination for disk A of $i_A \sim 65^\circ$, but did not resolve disk B and thus were unable to determine its inclination. They

found systemic LSRK velocities of 10.55 and 10.85 km/s for the two disks, which are close enough to be well within the escape velocity that the authors calculated for a disks at their projected separation of 440 AU of 2.5 km/s, indicating that the binary is bound. This similarity in systemic velocity also indicates that the binary's orbital plane is likely close to face-on.

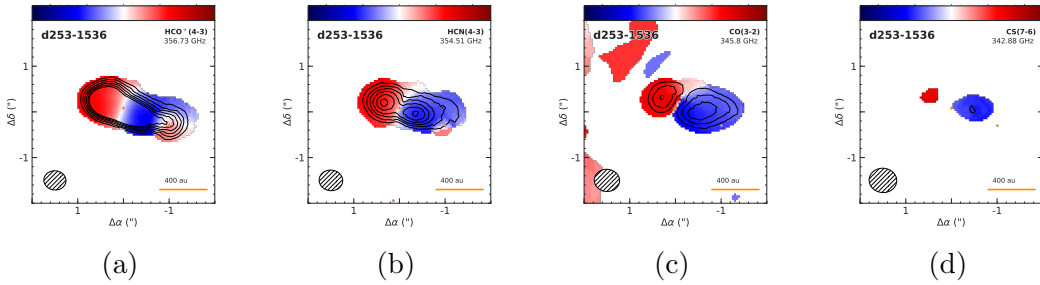


Figure 1.12: Moment-1 maps of HCO^+ (4-3), HCN (4-3), CO (3-2), and CS (7-6) emission (left to right) in the present study's proplyds. Each map shows intensity-weighted velocity, which allows us to trace the disks' kinematics. Observed with ALMA's Band 7 receiver

With our high resolution observations of gas line emission, we aim to determine the temperature, density, and chemical profiles of the system, as well as refining the mass estimates for both disks and host stars. With this information in hand, we will examine this disk's characteristics in the context of previously studied disks in the Taurus and ρ Ophiuchus star forming regions, as well as comparing it to the disk studied by Factor et al. (2017), and evaluate the disks' planet forming potentials.

1.4 Summary of Contents

In this work we characterize ALMA observations of two young protoplanetary disks in the d256-1536 system. Observations and data reduction are described in §2. In §3, data and basic analysis are presented. Descriptions of modeling and

fitting techniques are discussed in §4, and in §5, best-fit parameters are discussed and contextualized, as well as unexpected features maybe.

Chapter 2

Observations

The data presented in this thesis are part of an ALMA survey of Orion proplyds in Orion (project 2011.0.00028.S); data collection and analysis methods of the continuum results are presented in Mann et al. (2014). The observations were taken on October 24, 2012, in ALMA’s Band 7 receivers. Four spectral windows of width 1.875 GHz were arranged to cover the rest frequencies of the HCO^+ (4-3), HCN(4-3), CO(3-2), and CS(7-6) transitions (356.734 GHz, 354.505 GHz, 345.796 GHz, and 342.883 GHz, respectively). Each window was split into 3840 channels with a width of 488.28 kHz, yielding a velocity resolution of 0.42 km s^{-1} . Since this was part of a Cycle 0 Early Science project, the survey used only 22 of the ALMA’s 50 12 meter dishes in a hybrid configuration, with baselines ranging from 21.2 to 384.2 meters. This configuration yields a maximum angular scale of $8''$, angular resolution of $0.''5$, and beam FWHM of $15''$. At a Gaia-measured distance of 389 ± 7.97 (Gaia Collaboration et al. 2018,?)¹, max angular scales and angular resolution correspond to 3,112 AU and 194 AU, respectively. The observation’s pointing center was (05:35:25.30, -05:15:35.50). Each disk’s precise position was fit for (see §4), and are given in Table 2.1.

These data, from Field 4 of Mann et al. (2014) represent 13.6 minutes of on-source time. This duration was split into six 136 second observations, spaced out over 7.5 hours to ensure adequate *uv* coverage, yielding an RMS of 7mJy/beam

¹This measurement is nearer than the previous literature value of 414 pc.

Table 2.1: Disk Positions

Source	RA	Dec
d253-1536a	05 : 35 : 25.3002	-05 : 15 : 34.418
d253-1536b	05 : 35 : 24.2940	-05 : 15 : 35.800

in the line data. The resulting synthesized beam has dimensions of 0.57×0.51 arcsec with a position angle of 85° . Precipitable water vapor in the atmosphere was stable at 0.7 mm, indicating that atmospheric contributions to the data were negligible.

The data were calibrated by ALMA staff using standard procedures in the Common Astronomy Software Applications, or CASA (McMullin et al. 2007). The antenna-based complex gains and bandpass response of the system were calibrated using observations of the quasars J0607-085 and J0522-364 respectively. The absolute flux calibration was determined from observations of Callisto. The model of Callisto was drawn from Butler (2012). Absolute flux calibration is estimated to be accurate to within 10% (Mann et al. 2014).

The velocity reference frame was converted from CASA’s standard topocentric frame to LSRK (kinematic local standard of rest) using the CASA task `cvel`. Next, continuum emission was subtracted from the data in the uv plane using the CASA task `contsub`. Visibilities were imaged with standard inversion, deconvolution, and restoration procedures from the Multichannel Image Reconstruction Image Analysis and Display, or MIRIAD, package (Sault et al. 1995).

Chapter 3

Results

Spatially and spectrally resolved line emission was detected for CO (3-2), HCO⁺ (4-3), HCN (4-3), and CS (7-6) across around 50 channels of width 0.42 km s⁻¹. Here we present a discussion of these data, including line-emission statistics, diagnostic plots, and a consideration of the cloud contamination present.

Here are presented line-emission statistics, as well as moment maps, channel maps, and a discussion on the role of cloud contamination in the data.

3.1 Cloud Contamination

Cloud contamination occurs when emission from gas clouds along the observation's line of sight is detected. This is typically not a significant issue for observations of proplyds in low-mass star forming regions (SFRs), but since the Orion Nebula has a significantly higher gas density than those low-mass SFRs, cloud contamination presents problems in these data. This is particularly evident in the CO line, thanks to its low critical density and relatively high abundance in the background clouds, which allows it to excite and emit more readily than other molecules. As a result of higher critical densities and lower abundances, cloud contamination is less significant, but still present, in the other lines. It is crucial to manage and minimize the effects of this contamination before modeling so that our fitting algorithms do not try to model the cloud emission.

Luckily, there exist ways to minimize the effects of cloud contamination. To do so, we take advantage of the fact that the contaminating clouds tend to be very large relative to a proplyds and that, as discussed in §??, interferometers have the ability to filter by length scale. Using these two features, we may exclude a selection of the shortest baselines used in our data, effectively shrinking the largest angular scales and, consequently, significantly reducing the effects of the cloud emission.

To see whether or not we have cloud contamination, we may make a plot of RMS-noise against shortest baseline (by iteratively removing more and more of the short baselines). Were there no cloud contamination, we would find that this plot trends upwards (following the fact that noise is typically proportional to the inverse square root of amount of data). However, we can recognize the signature of cloud contamination if we find unexpectedly high noise at low baselines that falls off at longer ones. This decrease reflects the fact that, since the clouds are large, only the shortest baselines are significantly affected. This indicates that the ideal value to use as our minimum baseline length would be the inflection point at which the cloud contamination's contribution (decreasing with baseline length) gives way to the normal losses that come with decreasing signal (increasing with baseline length)¹. The results of making such plots are shown in Fig. ??.

From these plots, we find that excluding baselines less than 110 k λ , 80 k λ , and 60 k λ for HCO⁺, HCN, and CO, respectively, yielded optimum results. Since emission from the CS line already has a very low SNR and a higher critical density than the clouds can easily access, it showed minimal contamination and thus

¹Another way to justify the removal of data is to recall that, not only are these short baselines recording too much cloud emission, but they are also generally not sensitive to the disks, since they are too small for these short baselines to pick up. Therefore, losing them effectively removes noise without any consequence to the data we really care about.

Table 3.1: Integrated Flux Measurements with Baseline Cuts

Molecular Line	Baselines included	Max Angular Scale	Integrated Line Flux (Jy km s^{-1})	
			Disk A	Disk B
CS (7-6)	All	8.5	0.024 ± 0.02	[no detection]
CO (3-2)	All	8.4	[*]	[*]
CO (3-2)	$> 60k\lambda$	3.4	2.58 ± 0.47	1.85 ± 0.39
HCN (4-3)	All	8.2	0.80 ± 0.07	0.26 ± 0.08
HCN (4-3)	$> 80k\lambda$	2.6	0.69 ± 0.05	0.17 ± 0.08
HCO ⁺ (4-3)	All	8.2	5.79 ± 0.49	2.29 ± 0.56
HCO ⁺ (4-3)	$> 110k\lambda$	1.9	4.15 ± 0.31	0.80 ± 0.22

* Integrated line intensity was not calculated for CO(3-2) before the baseline cuts, as the data were too contaminated to give meaningful results.

excluding baselines did not improve the observations. Image statistics resulting from these cuts are presented in Table ??.

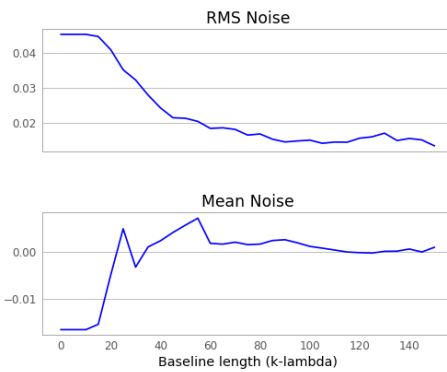
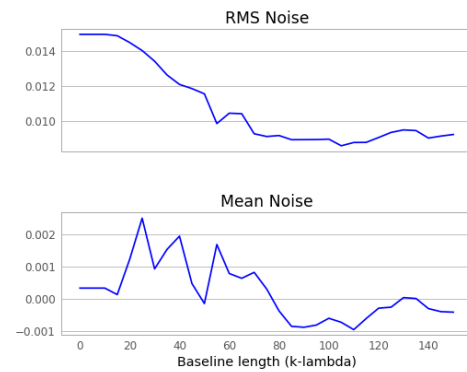
Figure 3.1: HCO⁺ Noise profiles

Figure 3.2: HCN Noise profiles

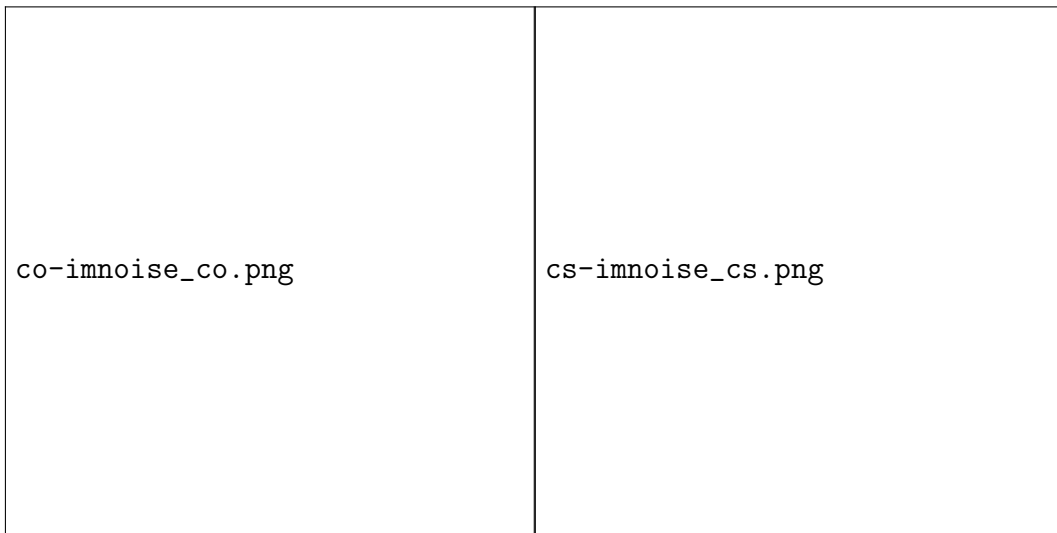


Figure 3.3: CO Noise profiles

Figure 3.4: CS Noise profiles

3.2 Line Data

Moment maps offer us ways to flatten the three-dimensional data-cube (in v, α, δ) into two dimensions. Moment 0 maps integrate flux along the velocity axis as a function of position, providing insight into structures of emission intensity in the disk's morphology, while moment 1 maps, a velocity-weighted intensity integration across position, present a source's velocity gradients. Figures 3.5 and 3.6 show zeroth- and first-moment maps, respectively, of the CO line emission, with and without a $60 \text{ k}\lambda$ baseline cut made (left and right, respectively).

Integrated line flux was measured using the Miriad task `cgcurs` to spatially integrate flux in a zeroth moment map over the region enclosed by the 3σ contour. The results of these measurements are shown in ???. From these values, we may estimate the disks' gas masses.

Assuming optically thin emission and Local Thermodynamic Equilibrium (LTE), the line-emitting gas mass, M_{gas} is given by:

$$M_{\text{gas}} = \frac{4\pi}{h\nu_0} \frac{Fmd^2}{A_{ul}X_u}, \quad (3.1)$$

where F is the integrated line flux, m is the mass of the emitting gas molecule, d is the distance to the source, h is the Planck constant, ν_0 is the molecular line's rest frequency, A_{ul} is the Einstein coefficient for the $(u - l)$ transition, and

$$X_u = \frac{N_u}{N_{\text{tot}}} = (2J_u + 1) \frac{\exp[-B_0 J_u (J_u + 1)hc/kT_{\text{ex}}]}{kT_{\text{ex}}/hcB_0}. \quad (3.2)$$

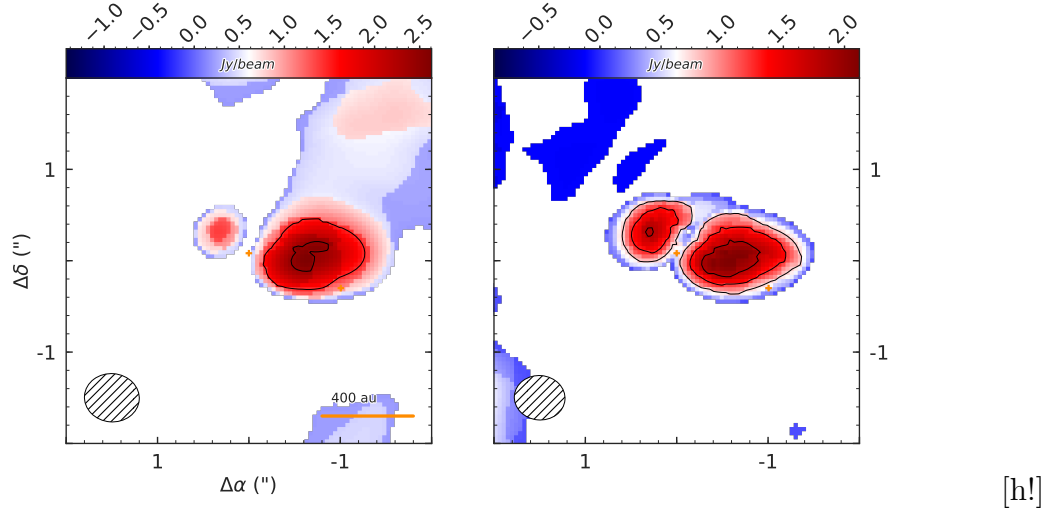


Figure 3.5: Zeroth moment map of CO emission, with and without a cut of all baseline's below $60 \text{ k}\lambda$ (left and right, respectively). Colors correspond to velocity-integrated intensity, while contours represent $\pm 3, 5, 7\dots 15\sigma$ transitions where 1σ is $0.257 \text{ Jy beam}^{-1} \text{ km s}^{-1}$. Negative contours are dashed. The beam is shown in the bottom left corner, with a diameter of $0.^{\circ}5$ which corresponds to 200 AU at 389 parsec.

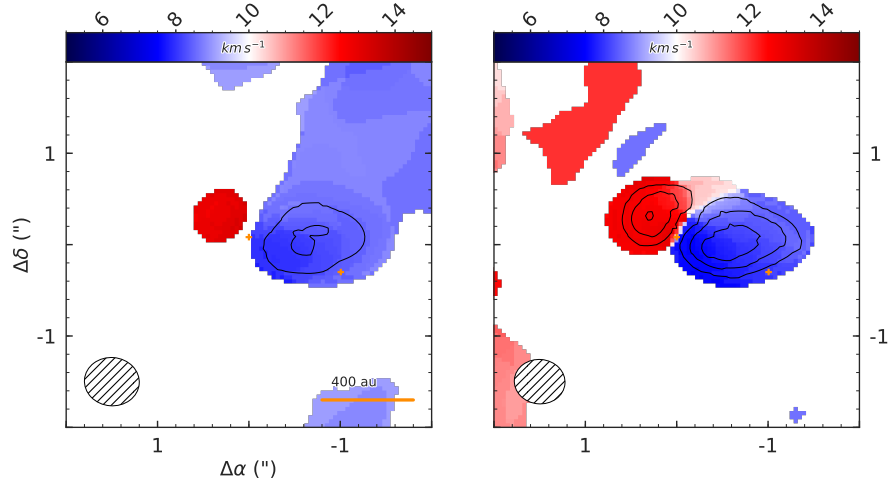


Figure 3.6: First moment map of CO emission, with and without a cut of all baseline's below $60 \text{ k}\lambda$ (left and right, respectively). Colors correspond to intensity-weighted LSRK velocity, while contours represent $\pm 3, 5, 7\dots, 15\sigma$ transitions where 1σ is $0.257 \text{ Jy beam}^{-1} \text{ km s}^{-1}$

Table 3.2: Values Used in Gas Mass Calculation
(HCO^+)

Parameter	Value	Max Source
F	$4.15 \text{ Jy km s}^{-1}$	Integrated line flux
J	4	NA
A_{4-3}	0.363	?
E_{4-3}	29.75 cm^{-1}	?
B_0	All	$B_0 = E_{4-3}/(\hbar c)$
T_{excite}	All	8.4
Distance	All	8.4
B_0	All	8.4

* Integrated line intensity was not calculated for CO(3-2) before the baseline cuts, as the data were too contaminated to give meaningful results.

In Eqn. 3.2, $\frac{N_u}{N_{\text{tot}}}$ is the ratio of the number of molecules in the upper state to the total number of molecules; J_u is the quantum number of the upper level; B_0 is the rotation constant in units of wavenumber; h and c are the Planck constant and speed of light, respectively; and T_{ex} is the excitation temperature. Values for A_{ul} and B_0 were taken from molecular data drawn from ?. The values used for this measurement are given in Table ???. Since Eqn. 3.1 is the mass of the observed gas species, it must be scaled by its relative abundance (fit for in Section 4) to obtain a total mass (*I'm not totally clear on this*). From this, we find a total mass of $0.x \pm 0.y M_\odot$.

A Position-Velocity (PV) diagram of the disk A's HCO^+ emission is presented in 3.7. The diagram shows the velocity distribution of emission along a slice along the disk's major axis. There is some noticeable asymmetry in the emission, both in terms of centroid intensity and in the extra feature at the eastern side of the map, which is likely the tail of disk B.

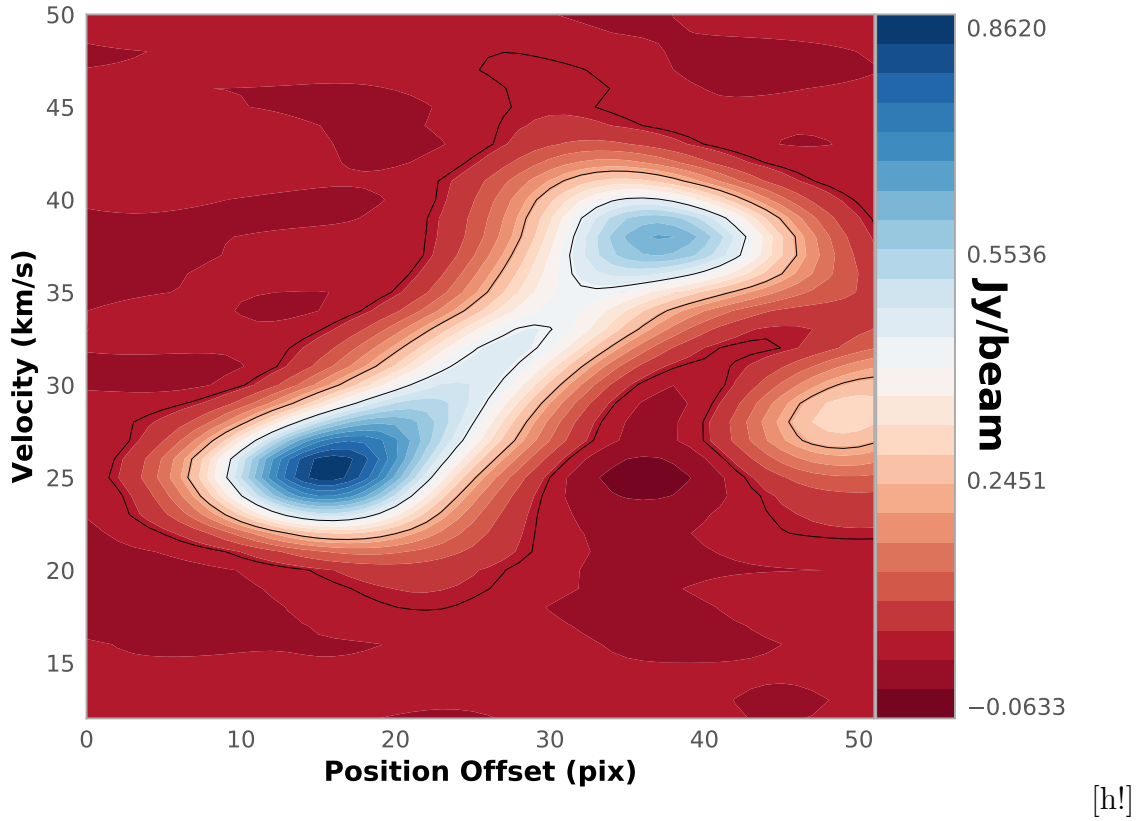


Figure 3.7: A PV diagram of disk A's HCO^+ emission. Some asymmetries are readily noticeable.

I don't know how valuable these PV diagrams are - is just having this one, of one disk in one emission line, sufficient, or should I make them for both disks in HCO^+ /both disks in all lines/something else? At this point, they're fairly easy to make, so the main cost would just be clutter.

Chapter 4

Analysis

By modeling spatially and spectrally resolved observations of protoplanetary disks, we can measure their chemical and physical characteristics. To model the system, we generate a synthetic image of what a disk with known physical characteristics (like disk radius, mass, and so on) would look like at a certain distance, inclination, and position angle relative to us. From that synthetic image, we may generate a synthetic set of visibilities, and then compare those visibilities to our observations. By iterating this process, we may generate many models with different parameter combinations and evaluate how well each resulting model disk matches our observations. We use a Markov Chain Monte Carlo technique described in §4.2.2 to explore the parameter space and measure the physical properties of the disk.

In §4.1, we describe the basic equations and computational processes that generate the model disks. In §4.2, we describe how, once models are made, we may move through high-dimensional parameter space to identify regions of best-fit. Finally, in §5.4, we present the results of our fitting procedures.

4.1 Gas Model

In this work, we use a gas-disk model originally developed by (Rosenfeld et al. 2012, 2013) and translated from IDL to Python by Flaherty et al. (2015). The

code assumes that Local Thermal Equilibrium¹ (LTE), and hydrostatic equilibrium. The code draws on user-input temperature- and surface-density profiles to calculate a vertical density structure, and calculates the velocity field based on the stellar mass. It then performs radiative transfer on the resulting structure to create a sky-projected image of the model disk, taking into account line thermal and turbulent line broadening. By assuming LTE and hydrostatic equilibrium, the code is able to run quickly enough to allow for a Markov Chain Monte Carlo routine to generate models on a reasonable timescale, as described in §4.2.2

4.1.1 Establishing Physical Profiles

A circumstellar disk can be characterized by three major profiles: its radial and vertical temperature structures, its radial and vertical density structures, and its velocity field. Generating a model disk is a matter of defining these three functions.

For the disk's temperature profile, we draw on the parametrization of disk temperature structure first laid out by Dartois et al. (2003), where the disk's temperature is given by,

$$T_{\text{gas}}(r, z) = \begin{cases} T_a + (T_m - T_a) \left[\cos \frac{\pi z}{2z_q} \right]^{2\delta} & \text{if } z > z_q \\ T_a & \text{if } z \leq z_q(r). \end{cases} \quad (4.1)$$

The atmospheric temperature and mid-plane temperatures are given by $T_a = T_{\text{atm},150}(r/150\text{AU})^q$ and $T_m = T_{\text{mid},150}(r/150\text{AU})^q$, where q is typically negative

¹This may or may not be a valid assumption in protoplanetary disks, but Pavlyuchenkov et al. (2007) showed that it was appropriate for CO.

and controls the functions' decay. Since T_m is smaller than T_a , the second term of the low-scale height temperature function is negative, so the sinusoid effectively implements a decreasingly-negative contribution to the temperature with height above midplane. The disk's scale height, controlled by z_q is assumed to be radially increasing, as described by a power law, $z_q(r) = z_{q,150}(r/150\text{AU})^{1.3}$. δ , a tunable exponent controlling the rate of the disk's vertical temperature decay, is set to 1, though it can take on values between 1-2 (Dartois et al. (2003)).

The disk's velocity field is assumed to be Keplerian with slight corrections for gas pressure support and the addition of a vertical dependence. The assumption of Keplerian velocities is generally valid in the case that $M_{\text{disk}} \ll M_*$, which continuum observations of the system have shown to be the case for the disks in this system (readers interested in a deeper explanation of the velocity field derivation are referred to Rosenfeld et al. (2013)). With these corrections added, the model disk's velocity field is given by

$$\frac{v_\phi^2}{r} = \frac{GM_*r}{(r+z)^{3/2}} + \frac{1}{\rho_{\text{gas}}} \frac{\partial P_{\text{gas}}}{\partial r}; \quad v_r = v_z = 0. \quad (4.2)$$

The final structure we would like to define is the gas density profile. By assuming hydrostatic equilibrium, we may relate the disk's gas density and temperature profiles as

$$-\frac{\partial \ln \rho_{\text{gas}}}{\partial z} = \frac{\partial \ln T_{\text{gas}}}{\partial z} + \frac{1}{c_s^2} \left[\frac{GMz}{(r^2+z^2)^{3/2}} \right]. \quad (4.3)$$

Here c_s is the local sound speed, given by $c_s^2 = \frac{k_B T_{\text{gas}}}{\mu m_H}$, T_{gas} is the temperature

profile given above, m_H the mass of hydrogen, and μ is the mean molecular weight of the gas, set here at 2.37 to reflect the gas's 80% H₂ composition. We may solve this equation by integration, giving us the disk's density profile $\rho(r, z)$.

The model's surface density profile is drawn from Hartmann et al. (1998), in which they expanded on the work of Lynden-Bell & Pringle (1974) to show that the structure of an isolated disk with viscosity given by $\nu \propto R^\gamma$ is well-described by

$$\Sigma_{\text{gas}}(r) = \frac{M_{\text{gas}}(2 - \gamma)}{2\pi R_c^2} \left(\frac{r}{R_c}\right)^{-\gamma} \exp\left[-\left(\frac{r}{R_c}\right)^{2-\gamma}\right], \quad (4.4)$$

where R_c is the radial extent of the gas disk, γ is a power law index, and M_{gas} is the total gas mass. This form allows the disk to behave as a power law radially until R_c , at which point it turns over into exponential decay. Hughes et al. (2008) showed that exponentially tapering the disk's outer radius, rather than sharply cutting it, provides the best agreement between gas and disk outer radii. We may safely approximate $M_{\text{gas}} = M_{\text{disk}}$, since at this early stage in the disk's development, the gas is by far the majority element of the disk's mass total.

Modifications are made to this density profile in two cases. At sufficiently low temperatures, molecules will condense out of the gas phase. The mid-plane of the disk is sufficiently cold to prompt this behavior. We may simulate this behavior by dropping the gas density by a factor of 10^{-18} wherever the temperature falls below some characteristic freeze-out temperature, T_{FO} , a temperature which is molecule-specific. Conversely, at the disk's upper surface, photodissociation by stellar and interstellar radiation dominates, so we implement a decrease in density wherever the hydrogen column density at the disk's surface falls below a characteristic value.

Table 4.1: Molecule-specific values

Parameter	Description	Fixed Value(s)	
		CO, HCO ⁺	HCN
T _{FO}	Molecular freeze-out temperature	19	60
σ _{Max}	Column density upper limit	[1.3 × 10 ³⁰] cm ⁻²	9.5 × 10 ²¹ cm ⁻²

* Values drawn from Factor et al. (2017)

We use values drawn from Factor et al. (2017) for these parameters, presented in Table 4.1. The resulting temperature and density structure of a typical proplyd is shown in Fig 4.1.

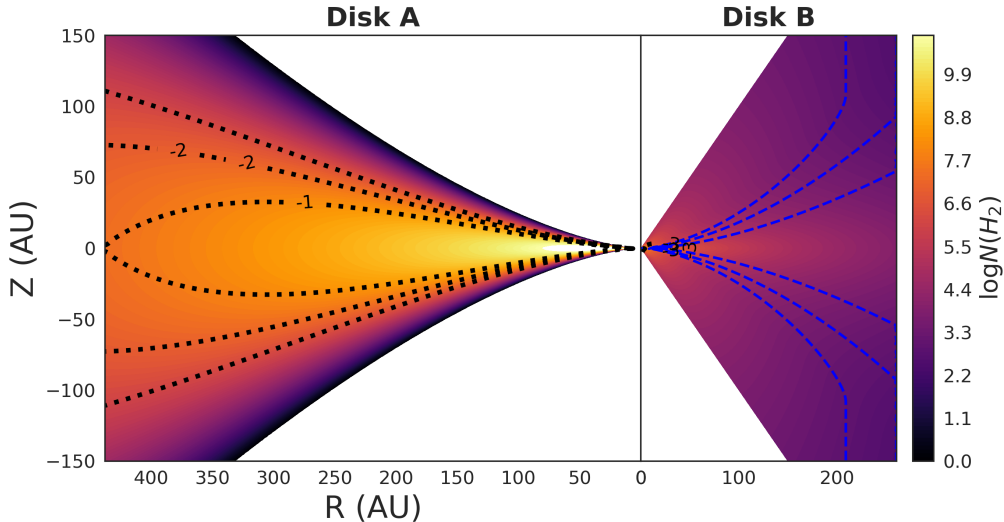


Figure 4.1: Radial and vertical temperature structures for disk A (*left*) and disk B (*right*) in CO. We may quickly see that disk A has a larger radial extent and a better defined profile, thanks to its higher signal.

4.1.2 Generating a Model Image

Having now established our model disk's physical structure through temperature, density, and velocity profiles, we may begin generating an image of the disk

by calculating flux contributions through the disk. To do so, we calculate the specific intensity by integrating the equation of radiative transfer:

$$I_\nu = \int_0^\infty K_\nu(s) S_\nu(s) e^{-\tau_\nu(s)} ds, \quad (4.5)$$

where $K_\nu(s)$ is the absorption coefficient, $\tau_\nu(s)$ is the optical depth and is defined as $\tau_\nu(s) = \int_0^s K_\nu(s')ds'$, and $S_\nu(s)$ is the source function. Since disks emit as blackbodies, the Planck function, $B_\nu(T)$, is used as the source function. Line broadening, a function of temperature and disk turbulence, is added, and the resulting flux is Doppler shifted to account for the disk's specified systemic velocity. Finally, the image is scaled, shifted, and rotated to account for the source's distance (d), angular offset from the center of the image ($\Delta\alpha$ and $\Delta\delta$), and position angle and inclination (PA and i) relative to our viewing direction.

Since the model disk is fully defined at every point in both physical and velocity space, we may set the spatial and spectral resolution to ensure that it is sampled well compared to the resolution of the data. We set our spectral resolution to match that of our observation, while we let the spatial resolution be $\sim 1/10$ the size of the synthesized beam. This resolution is high enough to avoid sampling artifacts when we simulate interferometric observations of the image.

We then use the Miriad task `uvmodel` to generate visibilities from the model image, sampled in the same *uv* tracks as our observation. The χ^2 statistic is then used as a goodness-of-fit metric to compare the data and model in the visibility domain. We make this calculation in the visibility domain, rather than the image domain, so that the resulting χ^2 value is not influenced by artifacts generated in the imaging process.

We now have the ability to generate a model disk, first by calculating its physical structures (in radial temperatures, densities, and velocities), then by drawing on radiative transfer to calculate the flux contributions from the disk. That flux is sky-projected to match the observed source's orientation, and the resulting image is then transformed from the image domain to the visibility domain and its fit quality evaluated.

4.2 Exploring Parameter Space

Now that we have the tools available to generate synthetic images that are tuneable across a large number of parameters, we must decide how best to move through that large parameter space to find a best-fit region. To do so, we use two methods.

4.2.1 Grid Search

The first, and perhaps most intuitive, way to move through this parameter space is using a simple grid search. A grid search involves manually assembling lists of values to try for each parameter and then generating models and calculating the resulting χ^2 value for every possible combination of parameters in those lists. A best-fit value is recovered by simply finding the point in that n -dimensional grid that yielded the best χ^2 , and then either calling that position in parameter space a best-fit location or then defining a finer grid around that point and repeating the process until an acceptable resolution has been reached. Benefits of grid search include its relatively straightforward nature (the the consequent simplicity of implementation) and its usefulness as a diagnostic tool, since very specific regions of parameter space may be sampled with the manual entry of positions to

test. However, it is a relatively simple method and leaves room for improvement.

Grid search was used to locate the disks in $(\alpha, , v)$ space. All other parameters were fixed at best-guessed values, then grids were run with resolutions sufficiently fine to meet the observations' spatial and spectral resolution. Grids for the disks' systemic velocities were centered at values found in Williams et al. (2014), while $\Delta\alpha$ and Δ offsets were first approximated using the MIRIAD task `uvfit` to fit a Gaussian to each disk. The resulting centroids were used to center the grids for refinement.

4.2.2 Markov Chain Monte Carlo

Markov Chain Monte Carlo (MCMC) algorithms offer us a way to both sample the probability distribution of a complex parameter space (much like a grid search), but offer an improvement over grid search by yielding the posterior probability distribution of each point, allowing us to characterize the uncertainty associated with each best-fit value with error bars. We use an affine-invariant formulation of the MCMC algorithm described by Goodman & Weare (2010) and implemented in the Python package emcee by Foreman-mackey et al. (2013).

MCMC routines sample the probability distribution of a given n -dimensional parameter space by deploying an army of "walkers." Each walker begins at some initial position, evaluates the χ^2 value of that point, and then proposes moving to a new position in parameter space according to a Gaussian probability distribution centered at the current point and decaying with distance (so that nearer points are preferentially - but not necessarily - selected). The χ^2 value of this new position - or "step" - is then evaluated, and is either accepted (the walker moves to that position) or rejected (the walker remains where it is and repeats the

new-step proposal process) with probability $p = \exp [(\chi_{\text{current}}^2 - \chi_{\text{new}}^2)/2]$ (is this only for Metropolis Hastings?). This function indicates that if the proposed step yields a better fit (a lower χ^2 value) than the current position, $p > 1$ and the step is accepted. However, if proposed step results in a worse fit, there is still a non-zero chance that the step is accepted, proportional to how much worse it is. This willingness to accept an increased χ^2 value allows the walker to avoid becoming trapped in local minima. The list of steps taken by each walker and their accompanying χ^2 values are compiled into the "chain" part of Markov Chain Monte Carlo. Goodman & Weare (2010) show that a walker's desire to remain in a location is proportional to the local probability density, meaning that we may infer uncertainties in our fits from the density of walker steps taken in a region.

We may introduce boundaries to the parameter space explored by our walkers using "priors." These priors are manually set, and allow us to restrict the walkers' motions into regions that we know a priori to be implausible fits. Justifications for these constraints are either mathematical (e.g. disk should not have a negative radius) or physical (e.g. both disks' radii are clearly far less than 1000 AU). These priors may be either uniform, with hard cuts at their bounds, or Gaussian, with preferential treatment given to walkers closer to the Gaussian centroid (a known value). For this work, we implement a Gaussian prior on each disk's position angle in order to guide the search towards the values reported in Williams et al. (2014) but still allow it the flexibility to self correct if necessary. This prior takes the form of a contribution to the log likelihood function, such that:

$$\ln \text{prob} = -\chi/2 - \ln \frac{1}{\sqrt{2\pi\sigma_{PA}^2}} \frac{\text{PA}^2}{2\sigma^2} \quad (4.6)$$

for each disk's position angle, where σ_{PA} is the position angle uncertainty given by Williams et al. (2014).

We may visualize the results of the walkers' journeys using corner plots. Corner plots allow high-dimensional space to be visualized in two dimensions by taking slices across each pair of axes and showing the density of samples drawn in that slice. In each of these slices, a perfectly certain fit would appear as a very tight, point-like Gaussian - the sample density around the best fit would be extremely high and low everywhere else, as the walkers quickly converged and remained on that best fit point - while conversely, higher uncertainties are shown by a wide spread of samples around the central point. Degeneracies between parameters can be seen as streaks in these corner plots, showing a correlation. Corner plots for Disk A and B in an HCO⁺ fit are shown in Figs 4.2a and 4.2b, respectively.

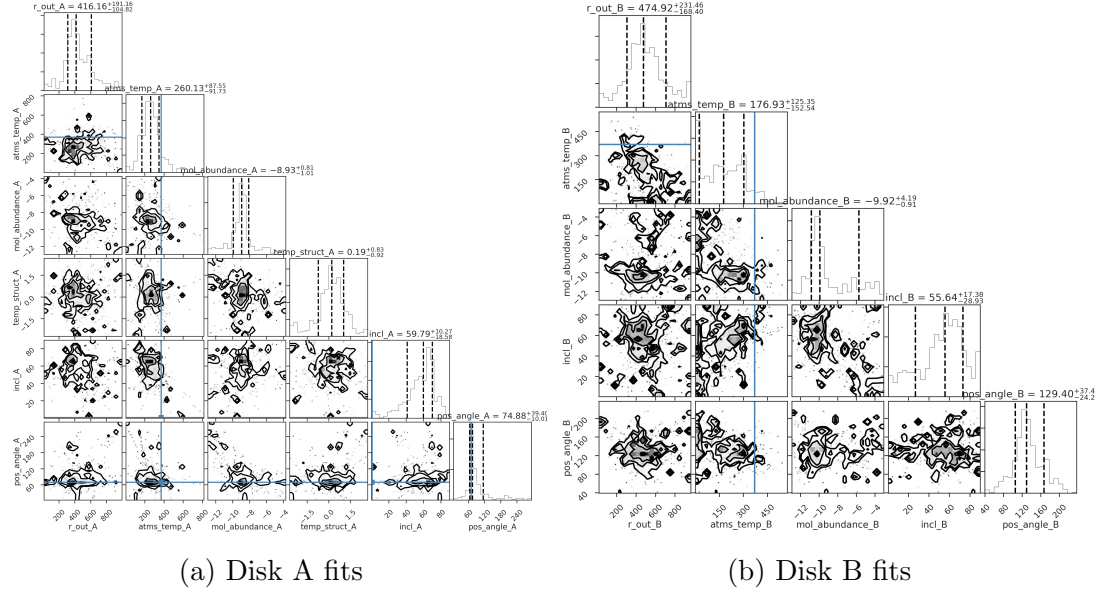


Figure 4.2: Since disk A and B's features are assumed to be independent, we may generate corner plots for each of their parameter spaces individually. Some analysis REWORK when new plots are added.

4.3 Fitting Procedure

Fitting of the data began with the analysis and partial removal of cloud contamination discussed in Section 3, resulting in the removal of baselines below a characteristic length for each line. With the data as clean as possible, position (α, δ) and velocity (v_{sys}) offsets were fit for. Offset fitting was executed only in the HCO⁺ line, thanks to the line’s minimal contamination and high signal strength. To fit these offsets, all other disk parameters were fixed at hand-selected, ballpark-reasonable values and a grid search was run over RA/Dec offsets and systemic velocities for each disk, using grid resolutions that corresponded to our observation’s spectro-spatial resolution. These grids were centered at values drawn from Williams et al. (2014), where fits were made to the disks’ continuum emission, but which proved to be in minor disagreement with our fitting. Positional offsets were confirmed with elliptical Gaussians in **CASA**. With these values established, they were treated as fixed parameters for the remainder of the fitting process.

Table 4.2 presents a list of parameters, including α, δ , and v_{sys} , which were left fixed throughout the MCMC runs. Since we are only modeling one line at a time, we are unable to constrain the vertical temperature structure and so fix T_{mid} and z_q . The selection of midplane temperature was made following Factor et al. (2017) to reflect the ”CO snow line” shown by Qi et al. (2011)², while the value of z_q was chosen, again following Factor et al. (2017), to be roughly double the disks’ scale heights, as shown in Rosenfeld et al. (2013). Since HCO⁺ is optically thin, temperature and density are degenerate, so γ is set at 1 following Andrews et al. (2009), who showed this to be a reasonable value for disks in ρ Ophiuchus.

²Although their measurements were made for sources in a different environment, the value gives us a reasonable starting point for our fits.

Table 4.2: Fixed Parameter Values

Parameter	Description	Source	Fixed Value (Disk A I)
$\Delta\alpha$ ('')	RA offset from image center	Grid-search, elliptical fit	0.0002
$\Delta\delta$ ('')	Dec offset from image center	Grid-search, elliptical fit	0.082
v_{sys} (km s $^{-1}$)	Systemic velocity	Grid-search	10.00
i ()	Inclination	Williams et al. (2014)	65
M_* (M_\odot)	Stellar mass	Williams et al. (2014)	3.5
v_{turb} (km s $^{-1}$)	Turbulence velocity	Flaherty et al. (2015)	0.08
d (pc)	Distance	Gaia Collaboration et al. (2018)	389
R_c (au)	Critical radius	Williams et al. (2014)	100
γ	Radial density power law index	Andrews et al. (2009)	1
z_q (au)	Disk scale height at 150 AU	Factor et al. (2017)	29
T_{mid} (K)	Midplane temperature at 150 AU	Qi et al. (2011)	19

Since our observations do not have enough spectral resolution to constrain the observations' turbulent linewidth, we fix v_{turb} at around 1% of the sound speed, per Williams et al. (2014).

The remaining parameters, presented and discussed in ??, are fit for using MCMC. We implement priors on each parameter, reported in Table 4.3. Gaussian priors are used for the fitting of both disks' position angles, centered at values presented by Williams et al. (2014), but which we would like to improve upon.

The result from the MCMC runs are presented below. To facilitate easier reading, figures are found at the end of the chapter.

Note: Everything below here is written kinda just as space filler, based off of the first 120 steps of each of the three fits. Still, if you could edit as though it is complete, I think that would be helpful for me to see, since I don't really know what I'm doing here!

Table 4.3: Fit Parameter Values

Parameter	Description	Prior
X_{mol}	Molecular abundance, relative to H_2 ^b	Uniform
q	Radial temperature power law index	Uniform
$T_{\text{atms}} \text{ (K)}$	Atmospheric temperature at 150 AU	Uniform
$M_{\text{Disk}} \text{ (M}_\odot)$	Log Disk mass ^c	Log Uniform

^a For the CO line, X_{mol} is fixed at the literature value of 10^{-4} .

^b For $\text{HCO}^+(4-3)$, HCN, and CS, disk mass was fixed at values from Williams et al. (2014).

4.3.1 $\text{HCO}^+(4-3)$ Fit

We began by fitting the HCO^+ line, using the MCMC methods explained above.

Best fit and median values with $1-\sigma$ uncertainties are given in Table 4.4, while corner plots, showing the posterior distributions of the individual line fit, is shown in Fig. ???. The corner plot shows that all parameters are fairly well constrained. I actually don't really see any degeneracies here?

Channel maps showing the data, best-fit model, and data-model residuals are shown in Fig. 4.8. Some residuals probably exist, and they probably line up with the CO contamination.

4.3.2 HCN (4-3) Fit

We proceed by next modeling HCN, following a similar path to the one taken for CO. As before, best fit and median values with $1-\sigma$ uncertainties are given in Table 4.5, channel maps are presented in Fig. 4.6, and corner plots are shown in Fig. ??.

In this run, we fix both disk's position angles at

Table 4.4: MCMC Fitting Results (HCO^+)

Parameter	Disk A		Disk B	
	Median	Best Fit	Median	Best Fit
X_{mol}	$-n_{-0.}^{+0.}$	-8.12	$-n_{-0.}^{+0.}$	-10.3
$r_{\text{out}}(\text{au})$	$-n_{-0.}^{+0.}$	333.86	$-n_{-0.}^{+0.}$	240.69
i ($^\circ$)	$-n_{-0.}^{+0.}$	[65]	$-n_{-0.}^{+0.}$	[45]
PA ($^\circ$)	$-n_{-0.}^{+0.}$	69.79	$-n_{-0.}^{+0.}$	121.22
q	$-n_{-0.}^{+0.}$	0.77	$-n_{-0.}^{+0.}$	[-0.5]
T_{atms} ()	$-n_{-0.}^{+0.}$	172.95	$-n_{-0.}^{+0.}$	183.17
lnprob			-28404.97	

* Values in [brackets] were fixed for this run.

For this line, the plots show that, while the solutions are generally unimodal, there are significant degeneracies between parameters. Most notable amongst these are the relationships between disk B's outer radius and its atmospheric temperature, molecular abundance, and position angle. These degeneracies are, in some sense, to be expected, since the disk is not resolved and so the MCMC struggles to differentiate between flux contributors.

A slightly more interesting pattern is found in the relationship between disk B's outer radius and disk A's atmospheric temperature, molecular abundance, temperature structure, and outer radius. This may be the result of the MCMC trying to make sense of the potential tidal feature linking the two disks, which is particularly noticeable in the HCN channel maps (relative to HCO^+ and CO). The bimodal hump in disk B's outer radius is a bit of a mystery to me, unless it represents the walkers' deciding to commit to either fitting or not fitting the tidal feature.

Table 4.5: MCMC Fitting Results (HCN)

Parameter	Disk A		Disk B	
	Median	Best Fit	Median	Best Fit
X _{mol}	-n _{-0.} ^{+0.}	-7.87	-n _{-0.} ^{+0.}	-11.09
r _{out} (au)	-n _{-0.} ^{+0.}	334.48	-n _{-0.} ^{+0.}	292.37
i (°)	-n _{-0.} ^{+0.}	[65]	-n _{-0.} ^{+0.}	[45]
PA (°)	-n _{-0.} ^{+0.}	70.05	-n _{-0.} ^{+0.}	134.2
q	-n _{-0.} ^{+0.}	0.62	-n _{-0.} ^{+0.}	[-0.5]
T _{atms} ()	-n _{-0.} ^{+0.}	125.68	-n _{-0.} ^{+0.}	388.21
ln Likelihood			-30928.35	

* Values in [brackets] were fixed for this run.

4.3.3 CO(3-2) Fit

We began by fitting the CO line. Since we fix CO's relative molecular abundance at $X_{\text{mol}} = 10^{-4}$, we may directly fit for the disks' masses and then use those values for the other lines.

The significant cloud contamination in the CO line presents difficulties for fitting. Since the contamination is most significant in the central five channels, those channels were not included in the fitting process. Although this degrades the

Additionally, maybe a tidal feature. Best fit values are reported in Table 4.6
Finally, we fit the CO(3-2) line. Fit results are summarized in 4.6, and visualized in ?? and 4.8.

Despite the removal of baselines below 60 km s^{-1} , the CO(3-2) line still shows significant cloud contamination in channels near the systemic velocity. In order to avoid having the MCMC walkers try to fit the contamination, we remove the channels with velocities between 9.88 and 12 km s^{-1} , which show the worst of the

Table 4.6: MCMC Fitting Results (CO)

Parameter	Disk A		Disk B	
	Median	Best Fit	Median	Best Fit
$\log M_{\text{Disk}}$ (M_{\odot})	$-n_{-0.}^{+0.}$	-0.29	$-n_{-0.}^{+0.}$	-4.9
r_{out} (au)	$-n_{-0.}^{+0.}$	437.71	$-n_{-0.}^{+0.}$	261.13
i ($^{\circ}$)	$-n_{-0.}^{+0.}$	65	$-n_{-0.}^{+0.}$	45
PA ($^{\circ}$)	$-n_{-0.}^{+0.}$	66.73	$-n_{-0.}^{+0.}$	[136]
q	$-n_{-0.}^{+0.}$	0.28	$-n_{-0.}^{+0.}$	[-0.5]
T_{atms} (K)	$-n_{-0.}^{+0.}$	5.54	$-n_{-0.}^{+0.}$	177.15
ln Likelihood				-33597.46

* Values in [brackets] were fixed for this run.

contamination. By choosing to not include these, we sacrifice some data, but the resulting fits are more representative of the structures we care about - the disks themselves - than they would be had we not sacrificed those channels.

Still, the resulting fits are noticeably less certain than those of the HCO+ and HCN lines, featuring several bimodal posteriors. Not really sure what to do about this. Manually cut some of them?



cornerplots-hco.pdf

Figure 4.3: Data, model, and residual maps are presented.

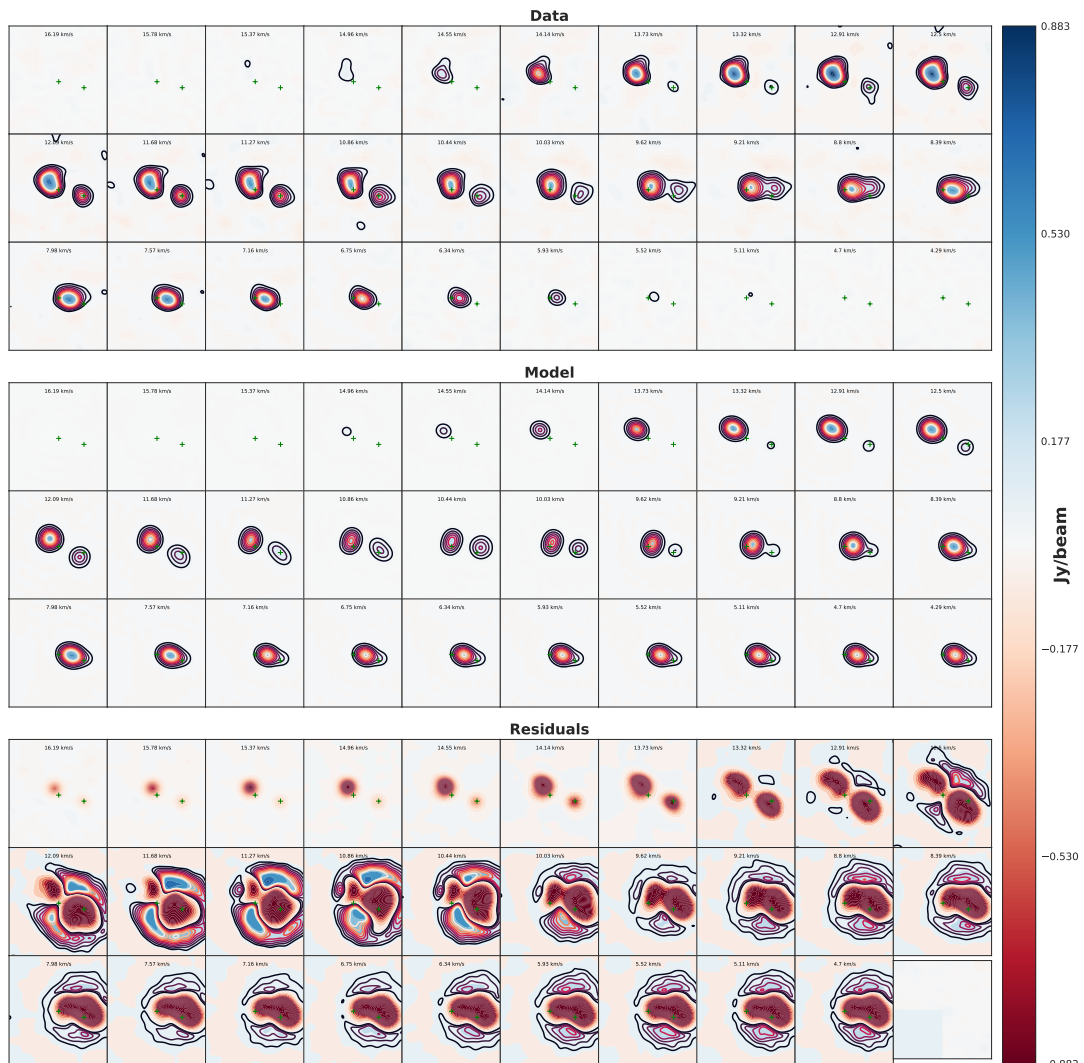
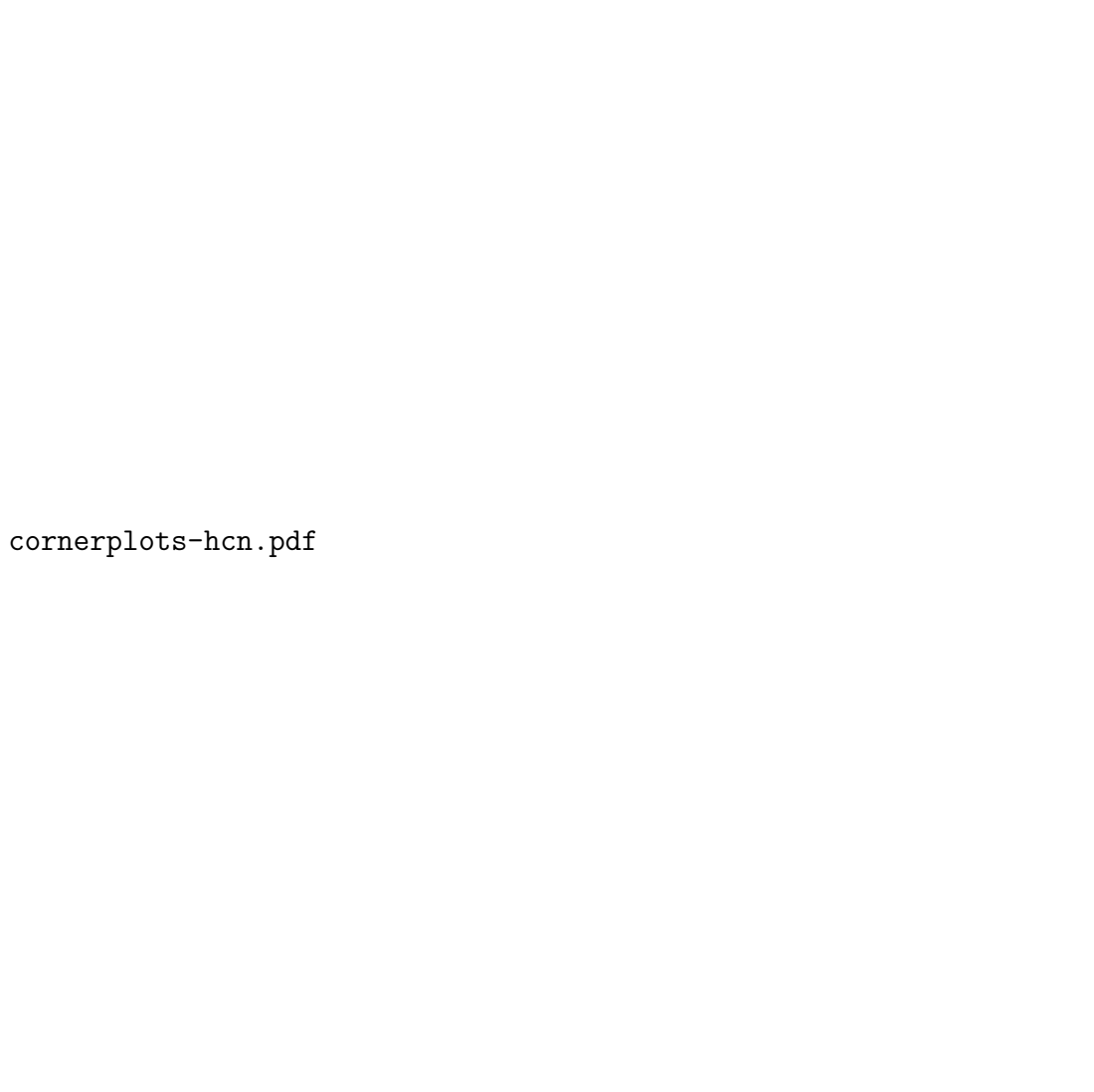


Figure 4.4: Data, model, and residual maps are presented.



cornerplots-hcn.pdf

Figure 4.5: Since disk A and B's features are assumed to be independent, we may generate corner plots for each of their parameter spaces individually. Some analysis REWORK when new plots are added.

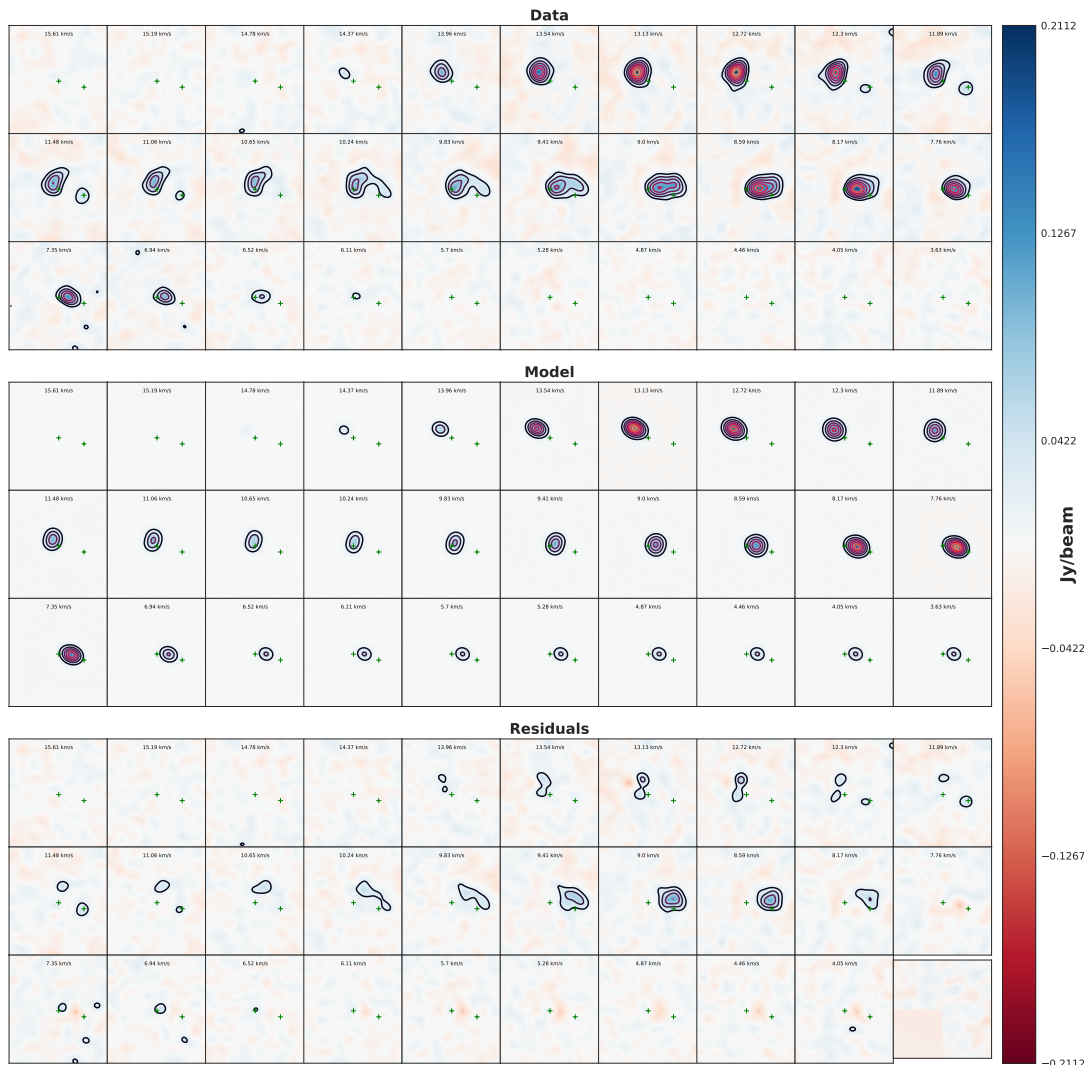


Figure 4.6: Since disk A and B's features are assumed to be independent, we may generate corner plots for each of their parameter spaces individually. Some analysis REWORK when new plots are added.



cornerplots-co.pdf

Figure 4.7: Since disk A and B's features are assumed to be independent, we may generate corner plots for each of their parameter spaces individually. Some analysis REWORK when new plots are added.

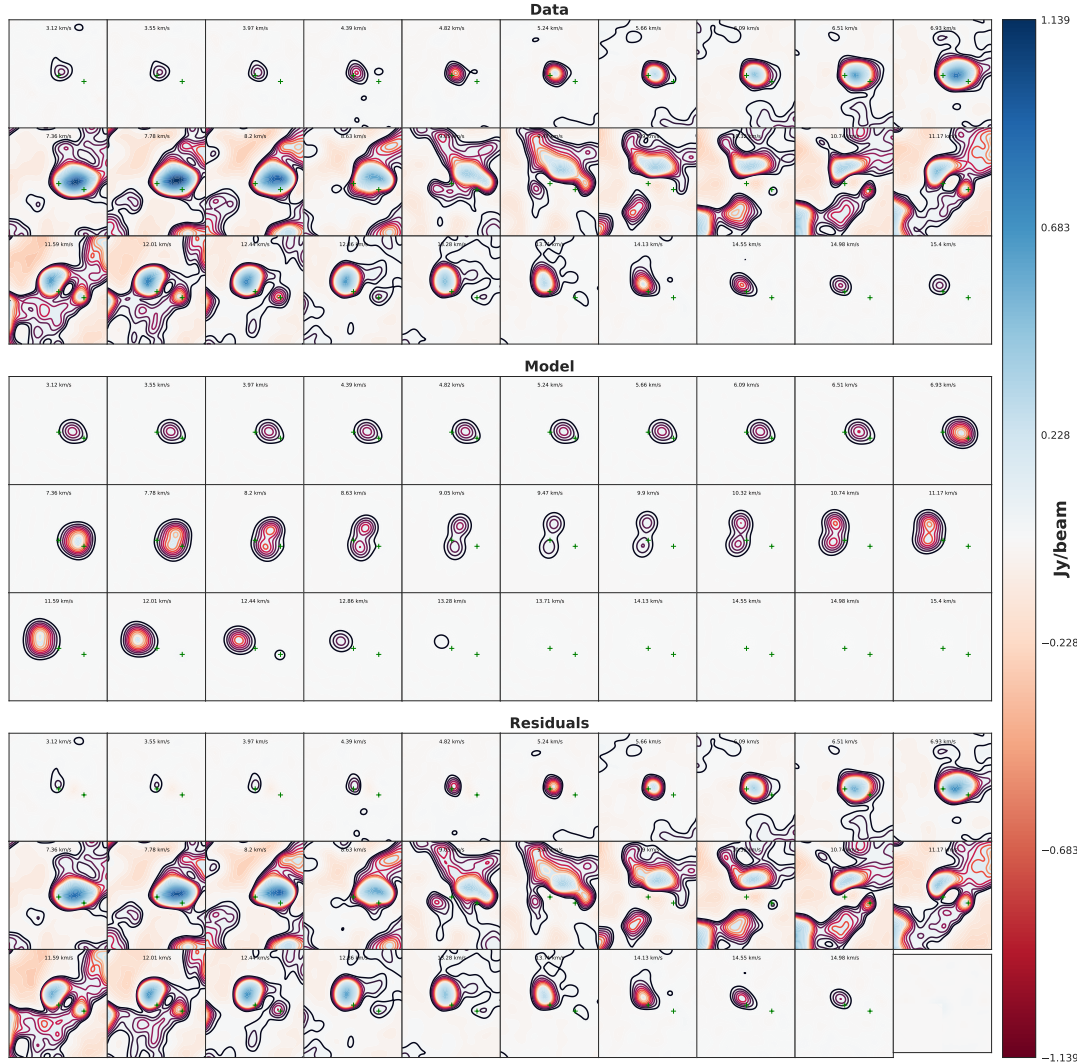


Figure 4.8: Since disk A and B's features are assumed to be independent, we may generate corner plots for each of their parameter spaces individually. Some analysis REWORK when new plots are added.

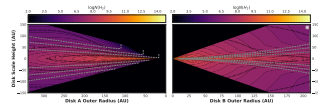


Figure 4.9: Disk structure

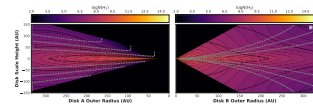


Figure 4.10: Disk structure

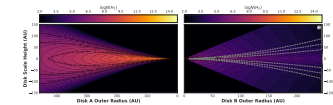


Figure 4.11: Disk structure

Chapter 5

Discussion

We find atmospheric temperatures notably higher than those found in Factor et al. (2017), in which analysis of the HCO⁺ line yielded an atmospheric temperature of 22K. Additionally, their negative radial temperature profile exponent (-0.22) is in disagreement with the positive value we find for Disk A here¹. This is notable, since Disk A's best-fit relative chemical abundance is also two magnitudes higher than the value of -10 that disk B's settled to and that they fixed theirs at. It seems strange that these would go together (i.e. that a higher atmospheric temperature, temp str, and abundance) would all go together, since all of them increase flux. A little strange? I dunno.

This could, however, reflect the fact that our fits do not include other temperature structure elements that Factor et al. (2017) fit for, most notably z_q and T_{mid} , which together control how the temperature structure decays vertically (see §4.1.1 for a more complete description).

5.1 Planet-Forming Potential

In order to gauge a disk's planet forming potential, we may begin by referring to the MMSN

One way to contextualize the results presented in §4 is through the lens of

¹Since disk B is unresolved, we are unable to fit its radial features.

planet formation. This analysis traditionally begins with a comparison to the MMSN, which is the density profile that our own Solar System would have if all our planets had gas added to them until their composition matched that of the Sun, then each planet’s mass was spread out in a ring along its orbital path (as discussed in §??). Integrating this mass leaves us with $M_{\text{MMSN}} \approx 0.01M_{\odot}$. It is worth reiterating that this is an extremely rough metric, build on several assumptions, and that it does not reflect *minimum* mass of a planet forming potential, but rather an approximation of the mass it would take for a disk like ours to form.

With the extremely large mass of $M = 0.36M_{\odot}$ that we measure in the CO line, it is needless to say that the disk’s mass would not be its limiting factor in planet formation.

Because we did not fit for the surface density profile index, instead option to leave it fixed at $\gamma = 1$ (Andrews et al. 2009),

5.2 Dynamical Mass of a PMS Star

5.3 Best Fit Temperature

5.4 HCO⁺, HCN Abundance Structures

Chapter 6

Summary

We have presented ALMA observations tracing line emission CO(3-2), HCO⁺(4-3), HCN(4-3), and CS(7-6) of d253-1536, a binary of young protoplanetary disks in the Orion Nebula Cluster. We use a gas model that assumes Keplerian rotation, local thermodynamic equilibrium, and hydrostatic equilibrium to develop synthetic images of the disks. We then use an affine-invariant Markov Chain Monte Carlo (MCMC) algorithm to explore parameter space and identify regions of best fit, comparing each model image to our data using a χ^2 test. By fitting each line's emission, we are able to statistically characterize the disks' density and temperature structures.

We compare these results to the one other ONC proplyd that has been characterized, as well as to other massive disks in the ρ Ophiuchus and Taurus clusters. We find that they are [TYPICAL/DIFFERENT].

Bibliography

- Aikawa, Y., & Herbst, E. 2003, *Astron. Astrophys.*, 371, 1107
- Anderson, K. R., Adams, F. C., & Calvet, N. 2013, *Astrophys. J.*, 774
- Andrews, S. M., et al. 2018, *Astrophys. J. Lett.*
- Andrews, S. M., & Williams, J. P. 2005, *Astrophys. J.*, 631, 1134
- . 2007, *Astrophys. J.*, 1
- Andrews, S. M., Wilner, D. J., Hughes, A. M., Qi, C., & Dullemond, C. P. 2009, *Astrophys. J.*, 700, 1502
- Ansdell, M., Williams, J. P., Manara, C. F., Miotello, A., Facchini, S., van der Marel, N., Testi, L., & van Dishoeck, E. F. 2017, *Astron. J.*, 153, 240
- Bontemps, S., et al. 2001, *Astron. Astrophys.*
- Bosman, A. D., van Dishoeck, E. F., & Walsh, C. 2018, *Astron. Astrophys.*
- Butler, B. 2012, ALMA Memo 594
- Chiang, E., & Laughlin, G. 2013, *Mon. Not. R. Astron. Soc.*, 431, 3444
- Cleeves, L. I., Bergin, E. A., Bethell, T. J., Calvet, N., Fogel, J. K. J., Sauter, J., & Wolf, S. 2011, *Astrophys. J. Lett.*, 743, 1
- Collaboration, T. E. H. T. 2019, *Astrophys. J.*, 1
- Combes, F., et al. 2018, *Astron. Astrophys.*, 79, 1
- Dartois, E., Dutrey, A., & Guilloteau, S. 2003, *Astron. Astrophys.*, 399, 773

- de Gregorio-Monsalvo, I., et al. 2013, *Astron. Astrophys.*, 557, A133
- Duchêne, G., & Kraus, A. 2013, *Annu. Rev. Astron. Astrophys.*, 1
- Dullemond, C. P., & Monnier, J. D. 2010, *Annu. Rev. Astron. Astrophys.*, 1
- Eisner, J. A., et al. 2018, *Astrophys. J.*
- Eistrup, C., Walsh, C., & van Dishoeck, E. F. 2017, *Astron. Astrophys.*
- F. Shu, F. Adams, S. L. 1987, *Annu. Rev. Astron. Astrophys.*
- Factor, S. M., et al. 2017, *Astrophys. J.*
- Flaherty, K. M., Hughes, A. M., Rosenfeld, K. A., Andrews, S. M., Chiang, E., Simon, J. B., Kerzner, S., & Wilner, D. J. 2015, *Astrophys. J.*, 813, 1
- Fogel, J. K., Bethell, T. J., Bergin, E. A., Calvet, N., & Semenov, D. 2011, *Astrophys. J.*, 726
- Foreman-mackey, D., Hogg, D. W., Lang, D., & Goodman, J. 2013, *Publ. Astron. Soc. Pacific*
- Gaia Collaboration. 2016, *Astron. Astrophys.*
- Gaia Collaboration, Brown, A. G. A., Vallenari, A., Prusti, T., de Bruijne, J. H. J., Babusiaux, C., & Bailer-Jones, C. A. L. 2018, *Astron. Astrophys.*
- Gaidos, E., Krot, A. N., Williams, J. P., & Raymond, S. N. 2009, *Astrophys. J.*, 696, 1854
- Goodman, J., & Weare, J. 2010, *Math. Sci. Publ.*, 5, 1
- Hartmann, L., Calvet, N., Gullbring, E., & D'Alessio, P. 1998, *Astrophys. J.*, 741

- Haworth, T. J., Boubert, D., Facchini, S., Bisbas, T. G., & Clarke, C. J. 2016,
Mon. Not. R. Astron. Soc., 463, 3616
- Henney, W. J., & O'Dell, C. R. 1999, Astron. J., 118, 2350
- Herrera-Martín, A., Hendry, M., Gonzalez-Morales, A. X., & Ureña-López, L. A.
2019, *Astrophys. J.*, 872, 11
- Hildebrand, R. 1983, Q. J. R. Astron. Soc., 24, 267
- Hogbom, J. 1974, *Astron. Astrophys. Suppl.*
- Hubickyj, O., Bodenheimer, P., & Lissauer, J. J. 2005, *Icarus*, 179, 415
- Hughes, A. M. 2010, PhD thesis, Harvard University
- Hughes, A. M., Duchene, G., & Matthews, B. 2018, *Annu. Rev. Astron. Astrophys.*, 1
- Hughes, A. M., et al. 2017, *Astrophys. J.*, 839, 86
- Hughes, A. M., Wilner, D. J., Qi, C., & Hogerheijde, M. R. 2008, *Astrophys. J.*
Johnstone, D., Hollenbach, D., & Bally, J. 1998, *Astrophys. J.*, 499, 758
- Kalyaan, A., Desch, S. J., & Monga, N. 2015, *Astrophys. J.*, 815, 112
- Kenyon, S. J., Gomez, M., & Whitney, B. A. 2008, *Handb. Star Form. Reg.* Vol.
I, I
- Kruijssen, J. M. D., & Longmore, S. N. 2019, 1
- Kuchner, M. J. 2004, *Astrophys. J.*, 612, 1147
- Lada, C. J., & Lada, E. A. 2003, *Annu. Rev. Astron. Astrophys.*, 57

- Luhman, K. L., Allen, P. R., Espaillat, C., Hartmann, L., & Calvet, N. 2010, *Astrophys. Journal, Suppl. Ser.*, 186, 111
- Lynden-Bell, D., & Pringle, J. E. 1974, *Mon. Not. R. Astron. Soc.*, 168, 603
- Mann, R. K., Andrews, S. M., Eisner, J. A., Williams, J. P., Meyer, M. R., Di Francesco, J., Carpenter, J. M., & Johnstone, D. 2015, *Astrophys. J.*, 802, 1
- Mann, R. K., et al. 2014, *Astrophys. J.*, 784, 1
- Mann, R. K., & Williams, J. P. 2009, *Astrophys. J.*, 699, 1994
- McKee, C. F., & Ostriker, E. C. 2007, *Annu. Rev. Astron. Astrophys.*, 565
- McMullin, J. P., Waters, B., Schiebel, D., Young, W., & Golap, K. 2007, *Astron. Soc. Pacific Conf. Ser.*, 376, 127
- Observatory, A. ????, *Origins — ALMA*
- Ovelar, M. d. J., Kruijssen, J. M. D., Bressert, E., Testi, L., Bastian, N., & Cabrera, H. C. 2012, 1, 1
- Pavlyuchenkov, Y., Semenov, D., Henning, T., Guilloteau, S., Pietu, V., Launhardt, R., & Dutrey, A. 2007, *Astrophys. J.*, 669, 1262
- Podio, L., et al. 2019, *Astron. Astrophys.*, 6, 1
- Qi, C., D'Alessio, P., Berg, K. I., Wilner, D. J., Hughes, A. M., Andrews, S. M., & Ayala, S. 2011, *Astrophys. J.*, 740
- Raymond, S. N., & Cossou, C. 2014, *Mon. Not. R. Astron. Soc. Lett.*, 440
- Reboussin, L., Wakelam, V., Guilloteau, S., Hersant, F., & Dutrey, A. 2015, *Astron. Astrophys.*, 579, A82

- Reggiani, M., Robberto, M., Da Rio, N., Meyer, M. R., Soderblom, D. R., & Ricci, L. 2011, *Astron. Astrophys.*, 534, A83
- Ricci, L., Robberto, M., & Soderblom, D. R. 2008, *Astron. J.*, 136, 2136
- Ricci, L., Testi, L., Williams, J. P., Mann, R. K., & Birnstiel, T. 2011, *Astrophys. J. Lett.*, 739, 1
- Robberto, M., et al. 2013, *Astrophys. Journal, Suppl. Ser.*, 207
- Rosenfeld, K. A., Andrews, S. M., Hughes, A. M., Wilner, D. J., & Qi, C. 2013, *Astrophys. J.*, 774
- Rosenfeld, K. A., Andrews, S. M., Wilner, D. J., & Stempels, H. 2012, *Astrophys. J.*, 806
- Sault, R. J., Teuben, P. J., & Wright, M. C. H. 1995, *Astron. Data Anal. Softw. Syst.*
- Schöier, F. L., van der Tak, F. F. S., van Dishoeck, E. F., & Black, J. H. 2005, *Astron. Astrophys.*, 432, 369
- Schwarz, K. R., Bergin, E. A., Cleeves, L. I., Blake, G. A., Zhang, K., Öberg, K. I., van Dishoeck, E. F., & Qi, C. 2016, *Astrophys. J.*, 0, 1
- Skilling, J., & Bryan, R. K. 1984, *Mon. Not. R. Astron. Soc.*, 211, 111
- Smith, N., Bally, J., Licht, D., & Walawender, J. 2005, *Astron. J.*, 129, 382
- Tachibana, S., Huss, G. R., Kita, N. T., Shimoda, G., & Morishita, Y. 2006, *Astrophys. J.*, 639, L87
- Tsiganis, K., Gomes, R., Morbidelli, A., & Levison, H. F. 2005, *Nature*, 435, 459

- van Dishoeck, E. F., & Blake, G. A. 1998, *Astron. Astrophys.*
- Vicente, S. M., & Alves, J. 2005, in *Astron. Astrophys.*, Vol. 205, 214–216
- Walsh, C., et al. 2016, *Astrophys. J.*, 823, L10
- Walsh, K. J., Morbidelli, A., Raymond, S. N., O'Brien, D. P., & Mandell, A. M. 2011, *Nature*, 475, 206
- Weidenschilling, S. 1977, *Astrophys. Space Sci.*
- Wernecke, S. J., & D'Addario, L. R. 1977, *IEEE Trans. Signal Process.*, 39, 1478
- Williams, J. P., & Cieza, L. A. 2011, *Astrophys. J.*
- Williams, J. P., et al. 2014, *Annu. Rev. Astron. Astrophys.*, 796
- Xiao, L., & Chang, Q. 2018, *Astrophys. J.*, 853, 22
- Yu, M., Evans, N. J., Dodson-Robinson, S. E., Willacy, K., & Turner, N. J. 2017, *Astrophys. J.*, 1